OXFORD

Cerebral Cortex, 2016, 1–22

doi: 10.1093/cercor/bhw143
Original Article

ORIGINAL ARTICLE

Distinct Functional Groups Emerge from the Intrinsic Properties of Molecularly Identified Entorhinal Interneurons and Principal Cells

Michele Ferrante[1,2,3], Babak Tahvildari[4,5], Alvaro Duque[4,5], Muhamed Hadzipasic[6], David Salkoff[4,5], Edward William Zagha[4,5], Michael E. Hasselmo[1,2,3] and David A. McCormick[4,5]

[1]Center for Memory and Brain, [2]Center for Systems Neuroscience, [3]Department of Psychological and Brain Sciences, Boston University, Boston, MA 02215, USA, [4]Department of Neurobiology, [5]Kavli Institute for Neuroscience, Yale School of Medicine, New Haven, CT 06520-8001, USA and [6]Interdepartmental Program in Neuroscience, Yale School of Medicine, New Haven, CT 06520-8001, USA

Address correspondence to Michele Ferrante, 2 Cummington Mall, Boston, MA 22015, USA. Email: mferr133@bu.edu; David A. McCormick, 333 Cedar Street, New Haven, CT 06510, USA. Email: david.mccormick@yale.edu.

Michele Ferrante and Babak Tahvildari are Co-first authors.

Babak Tahvildari was deceased, November 2013.

Michael E. Hasselmo is co-senior author.

Abstract

Inhibitory interneurons are an important source of synaptic inputs that may contribute to network mechanisms for coding of spatial location by entorhinal cortex (EC). The intrinsic properties of inhibitory interneurons in the EC of the mouse are mostly undescribed. Intrinsic properties were recorded from known cell types, such as, stellate and pyramidal cells and 6 classes of molecularly identified interneurons (regulator of calcineurin 2, somatostatin, serotonin receptor 3a, neuropeptide Y neurogliaform (NGF), neuropeptide Y non-NGF, and vasoactive intestinal protein) in acute brain slices. We report a broad physiological diversity between and within cell classes. We also found differences in the ability to produce postinhibitory rebound spikes and in the frequency and amplitude of incoming EPSPs. To understand the source of this intrinsic variability we applied hierarchical cluster analysis to functionally classify neurons. These analyses revealed physiologically derived cell types in EC that mostly corresponded to the lines identified by biomarkers with a few unexpected and important differences. Finally, we reduced the complex multidimensional space of intrinsic properties to the most salient five that predicted the cellular biomolecular identity with 81.4% accuracy. These results provide a framework for the classification of functional subtypes of cortical neurons by their intrinsic membrane properties.

Key words: cell functional classification, entorhinal cortex, grid cells, interneurons, intrinsic properties

Introduction

In the last two decades, large strides have been made in neuronal classification based on biomarkers, neuronal morphology, brain location, connectivity, and firing properties (Ascoli et al. 2008; Fishell and Rudy 2011; Rudy et al. 2011). Despite these advancements, understanding how neurons can be classified according to function remains a hard problem in neuroscience. Definitions for several types of intrinsic neuronal firing properties exist but neuroscience lacks a framework that allows an unbiased and unsupervised functional classification of neurons based on their intrinsic features. We implemented and applied such a method to analyze the intrinsic properties of molecularly identified neuronal populations in the entorhinal cortex (EC).

Principal cells in the superficial layers of the medial EC generate internal spatial representations, such as grid cell firing (Fyhn et al. 2004; Hafting et al. 2005) and border cell firing (Solstad et al. 2008). The morphological identity of Layer II grid cells has not been fully resolved, but a subset appears to be stellate cells (Domnisoru et al. 2013; Tang et al. 2014). Studies of Layer II principal cells show that stellate cells primarily interact through a network of inhibitory interneurons (Beed et al. 2013; Couey et al. 2013). This suggests a critical role for inhibition in generating grid cell firing. The intrinsic properties of entorhinal stellate cells (ST) and pyramidal cells (PYR) have been previously investigated (Alonso and Klink 1993; Dickson et al. 1997; Klink and Alonso 1997; Egorov et al. 2002; Erchova et al. 2004; Giocomo et al. 2007; Garden et al. 2008; Boehlen et al. 2010), but the same has not been done for EC inhibitory interneurons. Indeed, most of what is known about the classification, functions, and intrinsic properties of different interneuron classes in other brain regions has been applied to the EC but has not been directly investigated in the EC. Knowing the anatomical and functional diversity of interneurons in each brain region is important because GABAergic interneurons are believed to be critical modulators of local network dynamics. For example, rhythmic oscillatory activity is central to EC function and different interneurons may be selectively involved in supporting these oscillations (Pike et al. 2000; Cardin et al. 2009; Salkoff et al. 2015).

Three biomarkers, the Ca^{2+}-binding protein Parvalbumin (PV); the ionotropic serotonin receptor (5HTR3a); and the neuropeptide somatostatin (SOM), distinctly segregate nearly 100% of all cortical interneurons in three nonoverlapping classes (Lee et al. 2010; Rudy et al. 2011). PV^+ and SOM^+ interneurons embryonically derive from the medial ganglionic eminence, while $5HTR3a^+$ interneurons come from the caudal ganglionic eminence (Nery et al. 2002; Xu et al. 2004; Butt et al. 2005; Cobos et al. 2006; Lee et al. 2010; Miyoshi et al. 2010). In neocortex, the proportion of $5HTR3a^+$, PV^+, and SOM^+ interneurons is roughly equal, but PV^+ and SOM^+ cells are more prevalent in deeper layers, while $5HTR3a^+$ interneurons are more prominent in superficial layers (Rudy et al. 2011). PV^+ cells (e.g., basket cells) show the physiological properties commonly labeled as fast-spiking (FS) (Hu et al. 2014). Entorhinal cortical FS cells also coexpress regulator of calcineurin 2 (RCan2) (Tahvildari et al. 2012) (a gene encoding for a member of the RCan) that is used as a marker instead of PV in this paper. PV cells tend to be nonadapting, and prefer to target perisomatic regions of the postsynaptic cell (Klausberger et al. 2005). On the other hand, non-FS SOM^+ cells usually fall in the morphological category referred to as Martinotti-like and preferentially target the dendritic arbor of their postsynaptic cell. Finally, $5HTR3a^+$ interneurons tend to be the most physiologically and morphologically heterogeneous group of the three (Rudy et al. 2011).

The three main classes of cortical interneurons can be further partitioned (Rudy et al. 2011). For instance, $5HTR3a^+$ interneurons include two subtypes of cells, the Vasoactive Intestinal Polypeptide positive (VIP^+) cells and the NeuroPeptide Y positive (NPY^+) cells. NPY^+ cells can be subdivided even further into neurogliaform (NGF) and non-NGF (Non-NGF) (Karagiannis et al. 2009; Ibáñez-Sandoval et al. 2011). A much larger number of neocortical interneurons have been identified using electrophysiological properties and biomarkers at the Petilla convention (Ascoli et al. 2008). Neuronal functional classification is important as interneuron subclasses often exhibit consistent specialized functions across different cortical regions. On the other hand, it is also true that the same interneuron class may work differently across brain regions, examples of this phenomenon will be provided in this study. Together, the cells categorized as PV, SOM^+, NPY^+ NGF, NPY^+ Non-NGF, VIP^+, and $5HTR3a^+$ account for the vast majority of GABAergic cells in the superficial layers of either visual, frontal, or somatosensory cortices (Gonchar et al. 2008; Uematsu et al. 2008; Rudy et al. 2011).

The first goal of this study is to measure the intrinsic properties of all these classes of interneurons and their local principal cells in superficial layers of the EC of the mouse. The second goal is to provide a framework for functional classification of neurons in the brain that leverages information about cellular molecular identities and intrinsic properties. Previous attempts to characterize the intrinsic properties of medial (Canto and Witter 2012a) and lateral (Canto and Witter 2012b) EC neurons were performed in vitro and across different cortical layers based on morphological markers. The current study presents data comprehensively linking expression of specific molecular markers to cellular functional groups of principal cells and interneurons. In this regards, our data unveils a remarkable functional diversity between and within cell classes. This diversity hints at the computational richness of inhibitory networks involved in generating coding of spatial dimensions by EC neurons.

Materials and Methods

Datasets presented in this manuscript were collected simultaneously (from the same set of cells) with data presented in Tahvildari et al. (2012), which focused on interneuron activation during up- and down-states in EC. However, the physiological properties and data analysis presented here were not a component of the previous study.

Mouse Lines

Animal handling and experimental procedures were approved by the IACUC at Yale University and in agreement with NIH guidelines for the ethical treatment of animals. Five mouse lines were used to express either enhanced green fluorescent protein (EGFP), Zs-Green, or humanized Renilla green fluorescent protein (hrGFP) in specific interneuronal subclasses. These included 1) regulator of calcineurin 2 (RCan2) hemizygous [STOCK Tg (Rcan2-EGFP) EI79Gsat; stock number 010591-UCD; GENSAT]; 2) GIN (GFP-expressing Inhibitory Neurons; Oliva et al. 2000) homozygous [FVB-Tg(GadGFP) 45704 Swn/J; stock number 003718; The Jackson Laboratory] that are here referred to as SOM^+; 3) 5-hydroxytryptamine (serotonin) receptor 3a (5HTR3a) hemizygous [STOCK Tg(Htr3a-EGFP) DP271 Gsat; stock number 010546-UCD; GENSAT]; 4) NPY hemizygous [B6.FVB-Tg(Npy-hrGFP)1Lowl/J; stock number 006417; The Jackson Laboratory]; 5) VIP homozygous

mouse line expressing Cre under the VIP promoter [STOCK Viptm1 (cre)Zjh/J; stock number 010908; The Jackson Laboratory].

In order to characterize the passive and active intrinsic properties of FS interneurons, a mouse line was used that expresses the fluorescent marker EGFP under the control of the "regulator of calcineurin 2" (RCan2) promoter (Siddiq et al. 2001). As reported previously (Tahvildari et al. 2012), our whole-cell recordings in current clamp configuration revealed that all ($n = 32$) $EGFP^+$ cells in the EC of these animals showed electrophysiological properties typical for FS interneurons, and more than 85% of the reconstructed cells showed morphological properties typical of basket cells. Similarly, somatostatin expressing interneurons of Layers II/III of the EC were targeted using a transgenic mouse line expressing EGFP in a subpopulation of SOM^+ cells, known as GIN (Oliva et al. 2000).

For the RCan2, 5HTR3a, and NPY mouse lines, hemizygous males were crossed with wild-type females of the same background (Swiss Webster wild-type females for RCan2 and 5HTR3a mouse lines, and C57BL/6J for NPY mouse line). At postnatal Days 0–2, pups skulls were exposed to fluorescent illumination with an appropriate filter under a dissecting microscope (Discovery.V8; Nikon) to distinguish animals expressing green fluorescent protein (EGFP/hrGFP/Zs-Green) from wild-types. For selectively targeting Zs-Green expression in VIP cells, males and females of the VIP line were crossed with homozygous floxed Zs-Green mice [B6.Cg-Gt(ROSA)26Sortm6(CAG-ZsGreen1)Hze/J; stock number 007906; The Jackson Laboratory] to allow Cre-Lox recombination.

Brain Slices

Brain slices from the EC were obtained with a ~75° offset from the vertical plane (Fig. 1). Transgenic mice (male or female, 12–18 postnatal days) were anesthetized through injection of sodium pentobarbital (150 mg/kg) and beheaded. After craniotomy and brain extraction, the cerebellum and brainstem were severed with a surgical knife and the forebrain was placed in icy (~4°C) cutting solution (containing in mM: 85 NaCl, 75 sucrose, 25 $NaHCO_3$, 10 glucose, 3.5 $MgSO_4$, 3 myo-inositol, 3 Na-pyruvate, 2.5 KCl, 1.25 NaH_2PO_4, 0.5 $CaCl_2$, 0.5 L-ascorbic acid) and bubbled with 95% O_2 and 5% CO_2 with a final pH of 7.4. The forebrain was placed on its dorsal side and a custom knife guidance tool was used to perform a coronal cut, removing the rostral side of the brain (cut represented by the *D*–*V* axis line in Fig. 1). The brain was then placed in the same custom knife guidance tool,

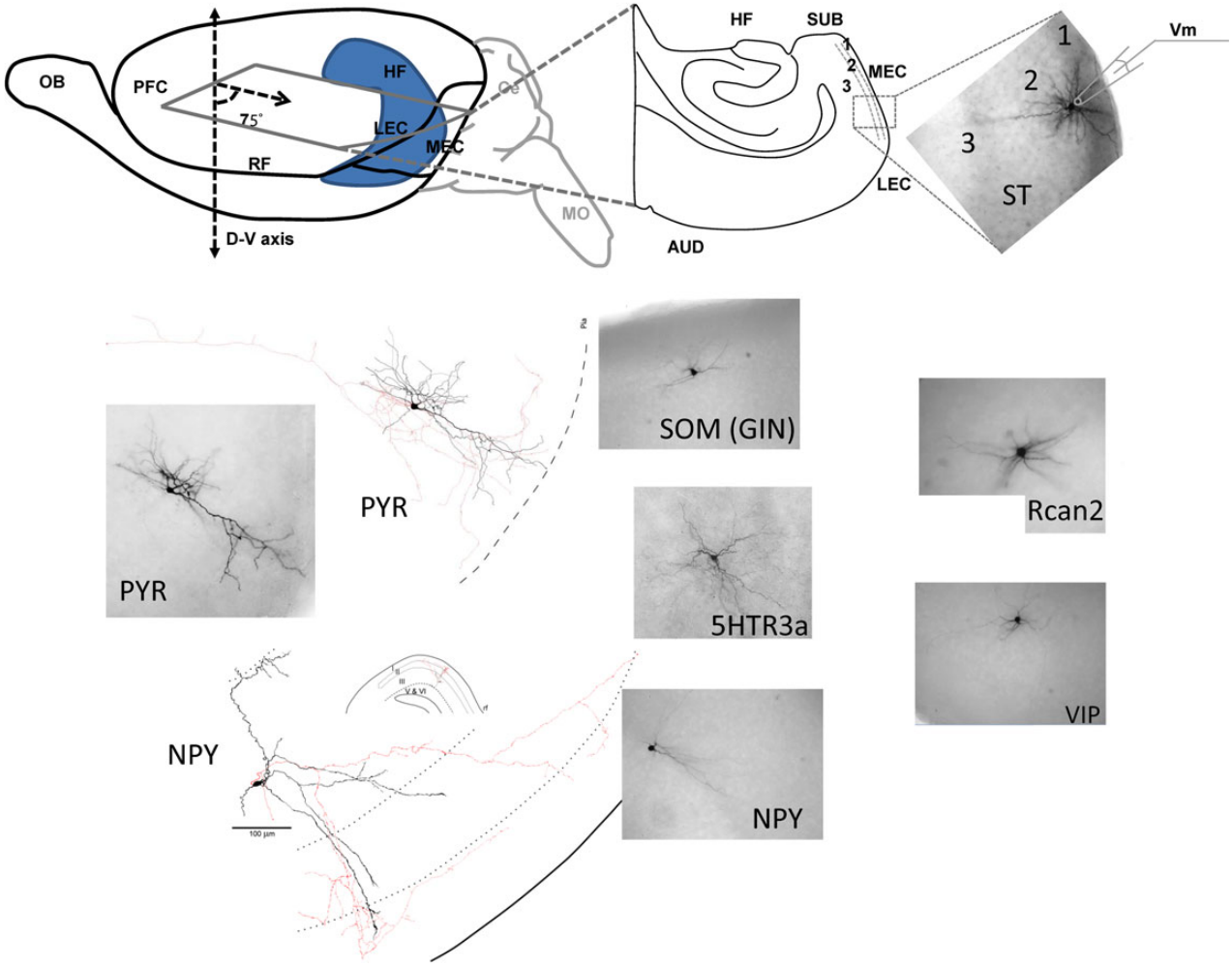

Figure 1. Cell identification, whole-cell recordings, and cell counts of distinct populations of EC interneurons and principal cells. Top left, schematic representation shows the semihorizontal slices cut at a 75° angle with respect to the *D*–*V* axis. Cerebellum (in gray) and rostral part of the brain were removed by coronal cuts. Top right, schematic of whole-cell recording from a single ST cell. Bottom, Examples of histological and morphological identification of distinct biocytin-filled cell classes and 3D morphological reconstruction.

on the rostral cut surface with the occipital lobe facing up and the dorsal neocortex was then cut at ~75° (posterior-to-anterior) with respect to the vertical plane (see Fig. 1). The brain was glued on its dorsal surface and positioned into an ice-cold vibratome (VT1000 S; Leica Microsystems). 320-μm-thick EC slices were obtained in ice-cold cutting solution and moved to an incubating chamber with ~35°C cutting solution for 30 min, followed by an additional 30 min at room temperature, then bubbled with 95% O_2 and 5% CO_2 in a holding chamber containing (in mM): 125 NaCl, 25 $NaHCO_3$, 10 glucose, 3 KCl, 3 myo-inositol, 3 Na–pyruvate, 2 $MgSO_4$, 2 $CaCl_2$, 1.25 NaH_2PO_4, 0.5 L-ascorbic acid.

Whole-Cell Recording

A brain slice was placed in an immersion recording chamber in the fixed-stage of an upright microscope (Axioskop; Carl Zeiss Microscopy) equipped with a mercury lamp, a near-infrared camera, and a 40× water-immersion lens. The slice was placed between two nylon nets (model: SHD-27LP/15 and SHD-41/15; Warner Instruments), allowing oxygenation and perfusion of the physiological solution on its upper and lower surfaces. To promote neuronal health in the slice we kept the flow rate of a well-oxygenated solution high (3–5 mL/min) (Hájos and Mody 2009; Tahvildari et al. 2012). The extracellular recording solution had the same chemical composition of the incubation solution except for the levels of calcium and magnesium, which were reduced to 1.2 and 1 mM, respectively. EC LII/III PYR cells were distinguished from ST cells based on the size and shape of their somata seen under near infrared-differential interference contrast (IR-DIC) microscopy. As previously reported (Suzuki 2010), EC LII and LIII were visually identified based on cytoarchitecture and distance from outer surface of the brain. In particular, LII was compact and its superficial border was detected based on the appearance of irregular distributed clumps of cells that were absent in LI. The deep border of Layer II was about 3 times deeper than the superficial border and was detected by the sparser appearance of Layer III. The deep border of Layer III was detected by the transition into LV which was densely populated. Epifluorescent light and DIC were used to visualize and target interneurons.

All whole-cell recordings were performed at ~32°C using a MultiClamp 700B amplifier (Molecular Devices) using borosilicate glass electrodes (World Precision Instruments) pulled on a Brown Flaming puller (model P-97; Sutter Instrument). Whole-cell current-clamp recordings were performed with 4–7 MΩ electrode resistance at the tip. The electrode was filled with (in mM): 130 K-gluconate, 10 Na-phosphocreatine, 10 HEPES, 7 KCl, 4 Mg-ATP, 0.3 Na-GTP, and 0.4% (w/v) biocytin. The pH was adjusted to 7.25 with KOH (pipette solution osmolarity was ~300 mOsm). A seal larger than 1 GΩ was established and negative pressure was applied to rupture the cell membrane. Firing properties of the recorded cells, as well as their input resistance and membrane time constant were investigated by injecting depolarizing and hyperpolarizing (500 ms) current step functions of different amplitudes. The electrode was then carefully removed from the recorded neuron and the brain slice was fixed with 4% paraformaldehyde in 0.1 M sodium phosphate buffer (NaPB) for at least 48 h at 4°C. Unless mentioned otherwise, all drugs and chemicals were purchased from Sigma–Aldrich.

Diaminobenzedine (DAB) Staining

Histochemical staining for biocytin was performed using procedures previously described (Tahvildari and Alonso 2005). Briefly, free-floating slices were removed from paraformaldehyde solution and washed in 0.1 M NaPB (three times for 5 min each). To suppress endogenous peroxidase activity, slices were incubated in 2% H_2O_2 in 0.1 M NaPB for 30 min, followed by 3 washes of 5 min each in 0.1 M NaPB. An additional 30 min wash in 0.1 M NaPB, 0.5% gelatin, and 0.4% Triton X-100 (PHT) was performed to prevent nonspecific binding. Then the slices were incubated with an avidin–biotin–horseradish peroxidase complex (Vector Laboratories) in 0.1 M NaPB and 0.4% Triton X-100 overnight.

The next day, the slices were washed extensively in PHT: 5 times (3 min each), then 1 time (30 min), then 6 times (1 h each), and finally overnight. Slices were then washed with 0.1 M Tris-buffered saline (TBS), pH 7.6 for 3 times (10 min each), and then transferred to 3,3-diaminobenzidine solution (DAB substrate solution) (Vector Laboratories). The DAB reaction was carried on by adding to 5.0 mL of distilled water 84 μL of Buffer Stock Solution, 100 μL of DAB Stock Solution, 80 μL of the Hydrogen Peroxide Solution, and 80 μL of the Nickel Solution. The DAB reaction was stopped when the desired staining intensity was reached by washing the slices in TBS 3 times (10 min each). Finally, the slices were mounted on glass slides, left to air dry for 5 min, and mounted with Mowiol (EMD Serono).

Fluorescent Staining and Antibodies Characterization

After postfixation, permeabilization, and blocking; free-floating brain sections (50 μm thick) were processed for either single or double labeling with mouse/rabbit anti-PV, -CR, -CB, -VIP, -SOM, or -NPY. After incubating in primary antibody for 48 h at 4°C, slices were washed 3 times (10 min each) in 1× PBS. The fluorescent secondary antibodies used in double-labeling experiments were donkey antimouse/donkey antirabbit Cy3 (Jackson Immunoresearch, West Grove, PA, United States of America) specifically, as in our previous study (Duque et al. 2013), the following antibodies were used: Mouse Anti-PV (Monoclonal, IgG1 Isotype; from Sigma); Mouse Anti-CR (Monoclonal, from Swant); Mouse Anti-CB (Monoclonal, from Swant); Rabbit Anti-NPY (Polyclonal, from Immunostar); Rabbit Anti-SOM (Polyclonal, from Immunostar); Mouse Anti-GABA (Monoclonal, IgG1 Isotype, from Sigma).

After 1 h incubation at room temperature, slices were mounted on gelatin-coated slides, air dried, and coverslipped with 2.5% D, L-2-amino-5-polyvinyl alcohol/1,4-diazabicyclo (2.2.2) octane (PVA-DABCO). Control sections were processed through the same immunohistological procedures, except that primary and secondary antibodies were not performed. In all cases, the omission of primary or secondary antibodies resulted in the lack of specific labeling, confirming the specificity of immunocytochemical analysis (Santi et al. 2006; Chen et al. 2009).

Neuronal Digital Reconstruction

The biocytin-filled cells were digitally reconstructed using the Neurolucida (MBF Bioscience, Williston, VT, United States of America) on a Nikon Zeiss microscope with a 100×objective. Digital neuronal reconstructions were then imported into CVAPP (Cannon et al. 1998) and postprocessed for data visualization. Original neuronal reconstructions, as well as postprocessed files are publicly shared through the NeuroMorpho.org database (Ascoli et al. 2007).

Electrophysiology

Data Analysis

Spike2 (Cambridge Electronic Design) or Clampfit 10 (Molecular Devices) was used to analyze the electrophysiological data. Graphs were created using Origin 8.0 (OriginLab Corporation),

MATLAB, Weka, Microsoft Excel, R, and Statistica. Values reported in the manuscript and graphs are mean ± SEM. Statistics were performed with either a *t*-test (for the two principal cell types, in Table 1) or two-way ANOVA with Šídák's correction for multiple comparisons (for the 6 interneurons, in Table 2). The same α value (0.05) was used for both tests. Hence, in this manuscript the word significant refers to statistically significant (with a $P < 0.05$), as reported in Tables 1 and 2.

Intrinsic Properties

Resting membrane potential was calculated as the average membrane potential (V_m) for the cell during a period of no network activity or electric stimulation. Apparent input resistance was estimated in current-clamp mode by applying a ~15 mV hyperpolarizing current pulse and dividing the exact voltage deflection (from the resting membrane potential) by the applied current. The membrane time constant was taken as the time to reach 63% of steady-state response. SAG ratio was calculated by applying a 25 mV (measured at the end of a 500 ms long) square hyperpolarizing current pulse to the cell and dividing the difference between voltage peak (V_p) and voltage steady-state (V_s) by the maximum voltage deflection during the pulse. AP-threshold was defined as the V_m when the rate of rise of the spike exceeded 15 V/s (as in Tahvildari et al. 2012), in response to a rheobase current pulse. AP-amplitude was calculated as the difference between the voltage at AP-threshold and the voltage at the peak of the AP. To compute the AP-duration (half-height-width) we measured the width of a spike at a voltage value equal to the AP-threshold plus half the AP amplitude. The dV/dt ratio was calculated as the minimum dV/dt value divided by the maximum dV/dt value during the AP. Adaptation index was calculated as the inverse of the duration between the last two spikes divided by the inverse of the duration between the first two spikes, with a current pulse stimulation equal to three times the rheobase. The amplitudes of spontaneous excitatory postsynaptic potentials (EPSPs) were calculated at rest and in the absence of slow oscillations. The EPSP amplitudes were computed as the absolute difference between the pre-EPSP resting membrane potentials and the EPSPs voltage peaks. These spontaneous EPSPs were likely a mix of compound and unitary EPSPs (i.e., quantal analysis was not performed to establish the average size of unitary EPSPs).

Our brain slicing method (described in Fig. 1) preserved the recurrent network connectivity necessary to produce a prototypical example of cortical slow oscillations (Steriade et al. 1993, 2001; Sanchez-Vives and McCormick 2000) (Supplementary Fig. 1A). In the EC, slow oscillations are characterized by synaptically driven Up states rhythmically followed by periods of network silence (Down states) (Tahvildari et al. 2012). Slow oscillations occur during slow wave sleep, anesthesia, drowsiness, and inattentiveness (Petersen et al. 2003) while the transitions to the awake and attentive states are characterized by loss of Down states and prolonged Up states (Steriade et al. 2001; Destexhe et al. 2010). Passive and active intrinsic properties were measured during Down states while synaptic properties (such as frequency and amplitude) were measured during Up states. The average duration of a slow oscillation cycle was 13.3 ± 0.95 s, 32% of the cycle was in the Up state.

Cluster Analysis

Cluster analysis was implemented using the software Statistica and an R package (Brock et al. 2008). For each EC interneuron recorded, data from the nine (active and passive) intrinsic properties described above were standardized. Then a tree clustering algorithm with a Euclidean distance metric and Ward's method amalgamation rule (Ward 1963) was used. The number of clusters was determined by examining the plot of Euclidean distance as a function of cluster stage (amalgamation schedule, Fig. 9A inset). The plot shows that the final large decrease in inter-cluster heterogeneity occurs from Stage 6 to 7, indicating that the resulting seven clusters are relatively homogeneous and that choosing a higher cutoff (lower number stage) would produce clusters lacking the same homogeneity. The cutoff is shown as a dashed line on the dendrogram in Fig. 9A.

For the decision or classification tree analysis (Fig. 9B1) we used equal prior probabilities to minimize the cost of predictive errors. Then, a parameter search was conducted using a regression tree that with the "FACT-style direct stopping" function determined the number of splits. Statistical differences in intrinsic properties between clusters of EC interneurons were calculated using a one-way ANOVA (α value, 0.05) with the Bonferroni correction for multiple comparisons. Finally, a heat map was used to visualize how many neurons of each class end up in each terminal node (Fig. 9B2).

Table 1 Passive and active properties of principal cells in LII/III of the EC

	n Firing pattern	PYR 18 Regular-adapting	ST 15 Regular-adapting
Passive properties	RMP (mV)	−75.4 ± 0.8* (−82 to −70)	−72.3 ± 0.7* (−78 to −68)
	Input resistance (MΩ)	242 ± 21* (125 to 400)	149 ± 16* (80 to 260)
	Time constant (ms)	34.5 ± 2.2* (22 to 60)	20.8 ± 2.8* (11 to 49)
	SAG ratio (%)	7.6 ± 0.7* (4 to 13)	31.9 ± 2.9* (7 to 53)
Active properties	AP-threshold (mV)	−53.8 ± 0.4 (−56 to −51)	−52.8 ± 0.8 (−58 to −43
	AP amplitude (mV)	88.6 ± 1.96 (68 to 98)	85.6 ± 1.2 (78 to 95)
	AP half-height-width (ms)	1.1 ± 0.04* (0.9 to 1.62)	0.98 ± 0.04* (0.52 to 1.24)
	dV/dt ratio (min/max)	−0.18 ± 0.01* (−0.24 to −0.13)	−0.22 ± 0.01* (−0.34 to −0.16)
	Adaptation (%)	27 ± 5*	35 ± 15*
	DAP	No	No 13; Yes 2
EPSP	ampl (mV)	8.5+2.9*	2.5 ± 1.2*
	Frequency (Hz)		

Values are reported in mean ± SEM.
RMP, resting membrane potential. DAP, depolarizing after-potential current.
*Statistically significant differences between neuronal classes ($P < 0.05$), *t*-test was used. Numbers in parentheses indicate the range (min–max).

Table 2 Passive and active properties of interneurons in LII/III of the EC

		A	B	C	D	E	F
		RCan2	SOM	5HTR3a	NPY–NGF	NPY–Non-NGF	VIP
	n	32	34	39	24	9	19
	Firing pattern	Delayed fast-nonadapting	Low-threshold -less adapting -thin spiking	Regular-adapting (but 1 FS, 1 DF)	Delayed regular-adapting	Low-threshold-adapting	73% regular 27% irregular adapting
Passive properties	RMP (mV)	$-78.5 \pm 0.6^{B-F}$ (−86 to −70)	$-70.7 \pm 0.5^{A,D,F}$ (−76 to −66)	$-71.7 \pm 0.6^{A,D}$ (−80 to −63)	$-75.5 \pm 0.8^{A,B,F}$ (−80 to −62)	$-74.1 \pm 1.4^{A,B}$ (−82 to −68)	$-71.4 \pm 0.8^{A,D}$ (−76 to −63)
	Input resistance (MΩ)	$156 \pm 8^{B-F}$ (60 to 250)	$452 \pm 28^{A,D}$ (190 to 800)	$432 \pm 29^{A,D}$ (200 to 900)	$206 \pm 11^{A-C,E,F}$ (130 to 340)	$385 \pm 58^{A,D}$ (200 to 720)	$508 \pm 43^{A,B}$ (250 to 900)
	Time constant (ms)	$9.9 \pm 0.7^{B,C,E,F}$ (5 to 23)	$39.6 \pm 3.7^{A,C,D}$ (15 to 98)	$28.5 \pm 1.4^{A,B,D,F}$ (17 to 52)	$11.3 \pm 0.5^{B,C,E,F}$ (8 to 16)	$34.6 \pm 2.4^{A,D}$ (25 to 44)	$38.5 \pm 2.6^{A,C,D}$ (19 to 60)
	SAG ratio (%)	$6.5 \pm 0.7^{B,C,E}$ (0 to 15)	$23.7 \pm 1.4^{A,C,D,F}$ (6 to 45)	$9.7 \pm 0.8^{A,B,D,E}$ (0 to 20)	$6.9 \pm 0.6^{B,C,E}$ (0 to 11)	$24.1 \pm 2.1^{A,C,D,F}$ (16 to 33)	$8.8 \pm 1.2^{B,E}$ (2 to 20)
Active properties	AP-threshold (mV)	$-48.1 \pm 0.6^{B,D-F}$ (−53 to −43)	$-51.5 \pm 0.5^{A,C,D,F}$ (−56 to −43)	$-48.7 \pm 0.5^{B,D-F}$ (−54 to −43)	$-43.5 \pm 0.6^{A-C,E}$ (−49 to −38)	$-52 \pm 1.1^{A,C,D,F}$ (−56 to −46)	$-44.3 \pm 0.5^{A-C,E}$ (−48 to −40)
	AP amplitude (mV)	$68.7 \pm 1.2^{B,D-F}$ (60 to 80)	$77.8 \pm 1.1^{A,C,D,F}$ (65 to 90)	$72 \pm 1.5^{B,D,F}$ (60 to 85)	$64.2 \pm 1.3^{A-C,E,F}$ (55 to 78)	$77.4 \pm 3.1^{A,D,F}$ (62 to 94)	$59.5 \pm 1.2^{A-E}$ (52 to 70)
	AP half-height-width (ms)	$0.48 \pm 0.02^{B-F}$ (0.3 to 0.7)	$0.71 \pm 0.02^{A,C-F}$ (0.46 to 0.95)	$0.98 \pm 0.03^{A,B,F}$ (0.6 to 1.3)	$0.99 \pm 0.04^{A,B,F}$ (0.6 to 1.35)	$0.93 \pm 0.08^{A,B,F}$ (0.65 to 1.45)	$1.19 \pm 0.04^{A-E}$ (0.95 to 1.6)
	dV/dt ratio (min/max)	$-0.44 \pm 0.01^{B-F}$ (−0.6 to −0.34)	$-0.36 \pm 0.01^{A,C,D}$ (−0.54 to −0.28)	$-0.27 \pm 0.01^{A,B,D,E,F}$ (−0.4 to −0.16)	$-0.3 \pm 0.03^{A-C}$ (−0.43 to −0.24)	$-0.37 \pm 0.02^{A,C}$ (−0.48 to −0.29)	$-0.33 \pm 0.02^{A,C}$ (−0.56 to −0.23)
	Adaptation (%)	$96.1 \pm 2.1^{B-F}$ (70 to 125)	$65.6 \pm 1.2^{A,C,D-F}$ (51 to 82)	$41.6 \pm 2.3^{A,B,E}$ (21 to 74)	$42.6 \pm 1.9^{A,B,E}$ (28 to 56)	$54.7 \pm 4.1^{A-D,F}$ (41 to 72)	$42.7 \pm 1.5^{A,B,E}$ (33 to 53)
	DAP	No 31; Yes 1	18 Yes; 16 No	No	No	7 Yes; 2 No	No

Values are reported in mean ± SEM. Statistically significant differences between neuronal classes are in superscript alphabet for $P < 0.05$ (see alphabetic key for neuronal classes on the top row). A two-way ANOVA with Šídák's correction for multiple comparisons was used. RMP, resting membrane potential; DAP, depolarizing after-potential current.

Results

EC LII/III Interneurons: Cell Counts

Immunohistochemistry was used to visualize biomarkers (e.g., PV, CR, CB, VIP, SOM, or NPY) (Supplementary Fig. 2) on our five genetically fluorescent classes of interneurons RCan2$^+$, SOM$^+$ (GIN), 5HTR3a$^+$, NPY$^+$, VIP$^+$. Each of the immunohistochemistry cell counts was repeated in anatomical preparations coming from at least two distinct animals to make sure results were consistent. This colabeling analysis suggested that some of our interneuron cell lines (Fig. 1) are nonoverlapping (Supplementary Fig. 2*B*). For instance, the 5HTR3a$^+$ line did not coexpress SOM or PV (which is also expressed in RCan2$^+$ cells) as very few double$^+$ cells were recorded (i.e., <2% of the 5HTR3a$^+$ cells expressed SOM or PV); the SOM$^+$ and NPY$^+$ lines did not express PV; and RCan2$^+$ cells did not express calretinin (CR) that is a marker largely coexpressed in VIP interneurons (Kubota et al. 1994; Porter et al. 1998). Not surprisingly, 80% of PV$^+$ cells coexpressed RCan2 (second bar graph in Supplementary Fig. 2*B*), as the two are common markers of FS cells. Also not surprisingly, all our SOM$^+$ (GIN) and NPY$^+$ cells expressed SOM and NPY, respectively, but our SOM$^+$ cells (whole-cell recording) only captured ~40% of the total SOM$^+$ population present in the EC, as the GIN line only expresses EGFP in a subset of SOM$^+$ interneurons (Oliva et al. 2000). Similarly, the NPY line (and therefore our whole-cell recordings) covered an even smaller subset of all the NPY interneurons in the EC, of the 179 immunoreactive NPY$^+$ cells only 14 (or 7.8%) were double positive. PV expression only begins at P10–P14 and fully matures at P25 (Doischer et al. 2008), hence it is normal that in our animals (P12–18) less than half of the Rcan2$^+$ cells coexpress PV. Unlike in other cortical regions (Rudy et al. 2011), where 5HTR3a cells are the most abundant group in the superficial layers, our results suggest that of all the GABAergic cells in the superficial layers of EC, RCan2$^+$ were the most numerous (26.4%), followed by 5HTR3a (21%), SOM (13.5%), and NPY (7.4%).

Our immunohistochemistry experiments detected GABA in 36.6% of the 5HTR3a$^+$ cells, 37.3% of the RCan2$^+$ cells, 49% of the SOM$^+$ cells, and 76.7% of the NPY$^+$ interneurons. Unfortunately, interpreting negative immunohistochemistry data are not a straight-forward process, because cells may express the marker that the immunohistochemical reaction is unable to detect experimentally (Dunstan et al. 2011), especially when detecting multiple biomarkers at the same time (i.e., double$^+$ cells). Hence, these results should not be interpreted as indicating that most of the 5HTR3a$^+$, RCan2$^+$, and SOM$^+$ are not GABAergic in nature.

PYR and ST Cells

Whole-cell recordings were used to analyze the basic electrogenic voltage responsiveness of 15 ST cells and 18 PYR cells. The EC principal cells were identified through morphological and physiological properties. The somas of ST cells (Fig. 2*A*) were mostly located in LII while the somas of PYR cells were mostly in LIII. PYR cells had basal dendrites mostly confined to the same layer of their somata and an apical trunk projecting to the most superficial layers (Fig. 2*D*). The dendrites of ST cells branched radially from a large soma and extended ~200 µm in every direction (Fig. 2*A*). Figure 2 shows the neurophysiological properties of stellate cells in response to hyperpolarizing current injection (Fig. 2*B1*,*B2*), and to suprathreshold current injection (Fig. 2*C1*,*C2*), as well as the response of pyramidal cells to hyperpolarizing (Fig. 2*E1*,*E2*) and depolarizing current injection (Fig. 2*F1*,*F2*).

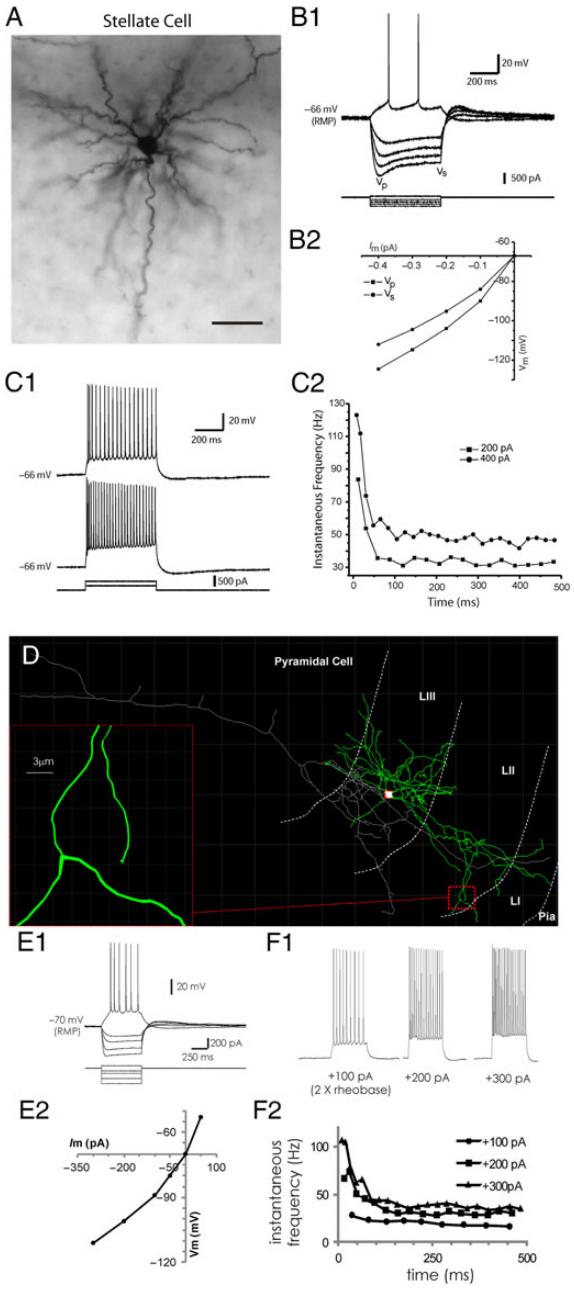

Figure 2. Intrinsic properties of ST and PYR Cells. (*A*) Morphology of a biocytin filled LII ST cell in the EC (scale bar = 15 μm). (*B1*) Examples of ST cell voltage responses to hyperpolarizing current steps of different amplitudes. Note large SAG response, shown by the difference between voltage peak (Vp) and voltage steady-state (V_s). (*B2*) Plot shows the voltage response (V_m) to hyperpolarized current steps of different amplitudes (I_m). The two lines represent voltage peak (Vp), and voltage steady-state (V_s), as in *B1*. (*C1*) Examples of ST cell spiking response to two suprathreshold current stimulations (200, 400 pA) lasting 500 ms each. (*C2*) Plot showing the time course of adaptation of the instantaneous firing frequency for the two current stimulations in *C1*. (*D*) A 3D reconstruction of an EC biocytin filled PYR neuron with soma (in white) located in LIII and dendrites shown in green and axon in gray. Inset (in red) depicts the magnified details of dendrites. (*E1*) Examples of PYR cell voltage responses to hyperpolarizing current steps of different amplitudes, note minimal SAG response. (*E2*) Plot shows the steady-state voltage response (V_m) to hyperpolarized current steps of different amplitudes (I_m). (*F1*) Examples of PYR cell spiking response to 3 suprathreshold current stimulations (+100, +200, +300 pA) lasting 500 ms each. (*F2*) Plot showing the time course of the instantaneous firing frequency adaptation for the three current stimulations in *C1*.

To the best of our knowledge, the intrinsic properties of ST and PYR cells have been previously compared in rats (Alonso and Klink 1993), and in macaque monkeys (Buckmaster et al. 2004) but not yet in mice as presented here. In several ways ST and PYR cells were similar; for instance, they both had firing patterns that could be characterized as regular-adapting. Also, the differences in AP-thresholds (Supplementary Fig. 3F) and AP-amplitudes (Supplementary Fig. 3I) between ST cells and PYR cells were not significant, but compared with the interneurons, principal cells exhibited the tallest spikes. However, the two principal cell types in the superficial layers of the EC also displayed several significant differences in intrinsic properties between each other and other cell classes (see Tables 1 and 2).

For instance, the average resting membrane potential (Supplementary Fig. 3A) of PYR cells is significantly more hyperpolarized (−75.4 ± 0.8 mV) than ST cells (−72.3 ± 0.7 mV) and input resistance in PYR cells (242 ± 21 MΩ) is significantly higher than ST cells (149 ± 16 MΩ) (Supplementary Fig. 3B). ST cells also have faster membrane time constants (20.8 ± 2.8 ms) than PYR cells (34.5 ± 2.2 ms) (Supplementary Fig. 3C). Analyzing the hyperpolarizing current-to-voltage (I/V) relationships for ST (Fig. 2*B1-2*) and PYR (Fig. 2*E1-2*) cells showed some key cellular differences. Upon application of a series of hyperpolarizing current step stimuli of different amplitudes, PYR cells showed a moderate-to-low amount of time-dependent inward rectification (Fig. 2*E1*, I_h-dependent SAG Ratio = 7.6 ± 0.7%) that was four times lower than that shown by ST cells (Fig. 2*B1*, SAG Ratio = 31.9 ± 2.9%, the highest among all recorded cell classes) (Supplementary Fig. 3D). These properties appears as a difference in the *I–V* curves for the initial (V_p) versus steady-state membrane potential (V_s) of stellate cells (Fig. 2*B2*) that did not appear in pyramidal cells (Fig. 2*E2*). Among all cell types, PYR cells (Fig. 2*F1-2*) were the most adaptive (low adaptation index) class (27 ± 5%) followed by ST cells (Fig. 2*C1-2*) that also tend to adapt pretty swiftly (35 ± 15% Table 1 and Supplementary Fig. 3G). Similarly, the dV/dt ratios of PYR cells (−0.18 ± 0.01) were the highest of all cell classes and were closely followed by ST cells (with −0.22 ± 0.01), indicating that the decay of the spikes was more gradual in EC principal cells than interneurons. Compared with all the other cell classes, ST cells, and PYR cells received the weakest (<1 mV amplitude) and lowest frequency (<40 Hz) EPSPs during Up states (Supplementary Fig. 1B).

RCan2 Interneurons: A Homogenous Group of FS Cells

Morphological reconstructions (Fig. 3A) showed that RCan2 cells had dense axonal arborizations mostly confined to the same layer of their somata and dendrites whose diameters tapered with distance from the soma while extending to more superficial layers. FS (e.g., RCan2$^+$) inhibitory interneurons are typically basket or chandelier cells (McCormick et al. 1985; Kawaguchi et al. 1987; Kawaguchi and Kubota 1997). Of the 32 RCan2$^+$ interneurons recorded, 27 had basket cell morphologies, while we identified the rest as putative chandelier cells. Moreover, RCan2$^+$ interneurons had some distinctive passive and active membrane properties (Supplementary Fig. 3 and Table 2) that significantly differentiated them from other types of interneurons, in agreement with studies of FS cells outside of EC. In terms of passive membrane properties, RCan2$^+$ interneurons had the most hyperpolarized resting membrane potential (−78.5 ± 0.6 mV; range = −70 to −86 mV, Supplementary Fig. 3A), and the lowest input resistance (156 ± 8 MΩ; range = 60–250 MΩ, Supplementary Fig. 3B). In terms of active membrane properties, RCan2$^+$ interneurons had the shortest AP width measured at the half-height (0.48 ± 0.02 ms; range = 0.3–0.7 ms,

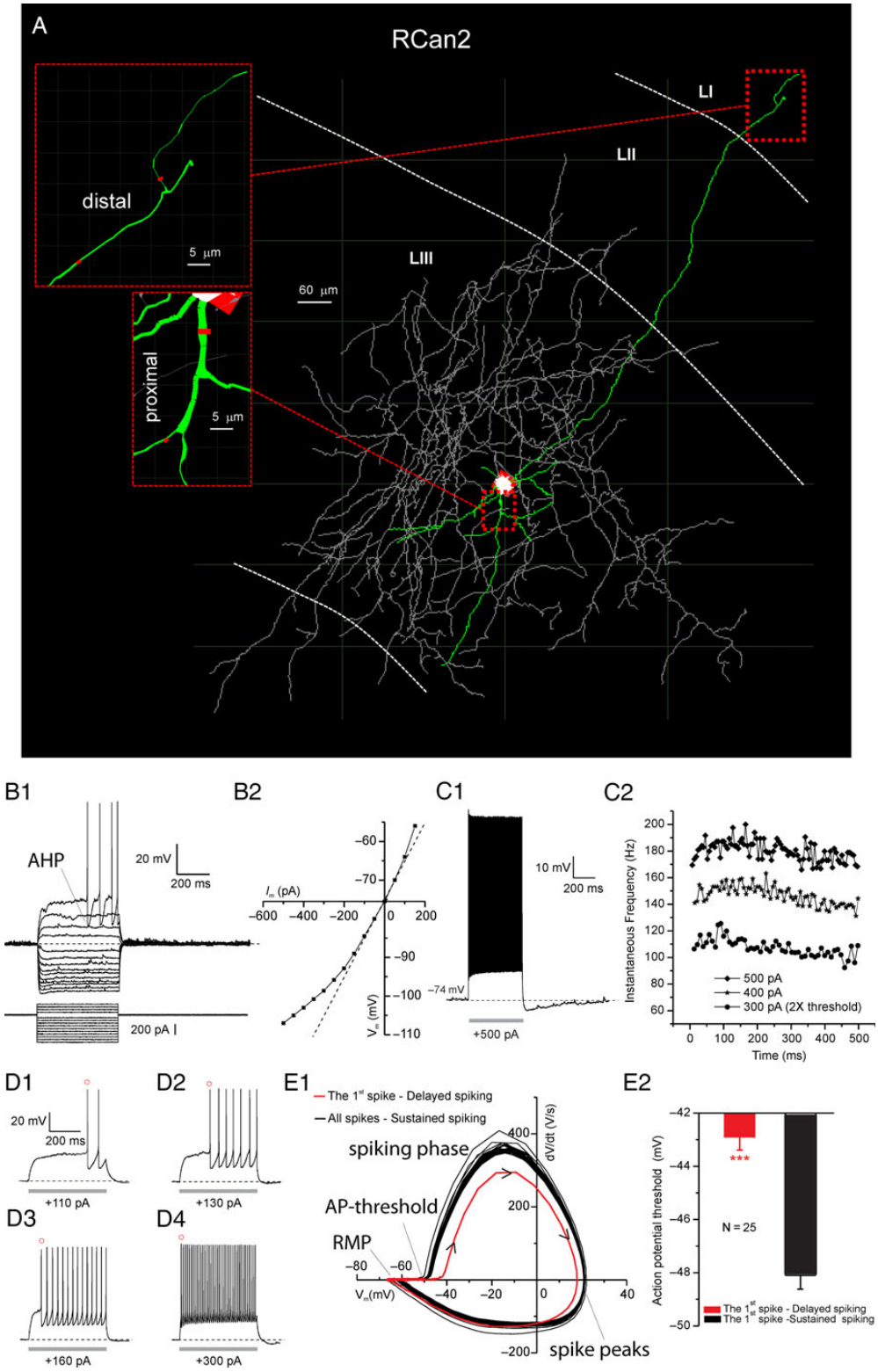

Figure 3. Intrinsic properties of RCan2$^+$ interneurons. (*A*) Neurolucida 3D reconstruction of an EC RCan2$^+$ interneuron with dendrites (in green), soma (in white), and axon (in gray). Insets show fine morphological details (e.g., branch diameter, in red) for proximal and distal branches. (*B1*) Voltage responses to a series of hyperpolarizing and then depolarizing current pulses up to rheobase. Note the large fast AHP characterizing this class of interneurons. (*B2*) Current–voltage (*I–V*) relations for each voltage response in *B1*. (*C1*) Characteristic RCan2$^+$ spiking response to suprathreshold current injection. (*C2*) Time course of the spike-frequency adaptation for 3 samples of input currents. (*D1–4*) Delay of the first AP as function of the stimulus amplitude. Note AHP becomes smaller as the stimulus strength increases. (*E1*) Phase plot depicting the phases of the somatic spikes from the resting membrane potential (RMP), to the AP-threshold, through the spiking phase and spike peak all the way back to the RMP. Kinetics of the first AP shown in red with black arrow heads showing the direction of the temporal progression of the spike. (*E2*) Significant difference in the voltage threshold for the first and subsequent APs.

Supplementary Fig. 3E) the smallest values of the minimum to maximum dV/dt (–0.44 ± 0.01%; range = –0.34 to –0.6%, Supplementary Fig. 3H), and also the largest adaptation index (96.1 ± 2.1%, ranging from 70 to 125%, Supplementary Fig. 3G) indicating almost no adaptation on average. Both the short AP width and the large adaptation index of the RCan2$^+$ cells were significantly different from those of the other cell types recorded.

Analysis of the current/voltage (*I*/*V*) relationships (Fig. 3*B2*) also revealed a series of physiological differences characterizing RCan2$^+$ interneurons. RCan2$^+$ cells showed a negligible amount of time-dependent inward rectification upon application of a series of hyperpolarizing currents of different intensities (SAG Ratio = 6.5 ± 0.7%; range 0–15%). However, all the recorded RCan2$^+$ neurons showed a clear instantaneous inward rectification toward hyperpolarizing and depolarizing membrane potentials, as reflected by the upward bending of the instantaneous *I*/*V* curve toward the negative and positive ends, respectively (Fig. 3*B2*). We also observed that most RCan2$^+$ neurons in LII/III of the EC (30 out of 32) showed a prominent delay of the first spike from the onset of the near threshold stimulus (Fig. 3*B1* and *D1-3*), as previously reported in supragranular layers of other neocortical regions (Goldberg et al. 2008). Duration of this delay was gradually reduced by injecting slightly larger (10–30 pA increments) depolarizing current step pulses (Fig. 3*D1–4*). Furthermore, we observed that when we stimulated RCan2$^+$ interneurons with depolarizing step currents of much larger intensity (e.g., 2× threshold or larger), they continuously discharge trains of brief APs at high frequency with a very small amount of frequency adaptation (96.1 ± 2.1%) (Fig. 3*C1–2*). RCan2$^+$ interneurons also showed pronounced after-hyperpolarization (AHP) when spikes were elicited right above the AP-threshold (Fig. 3*B1*). The AHP became less noticeable with more depolarized stimuli (Fig. 3*C1*,*D1–4*). The phase-plot graph of the voltage (Fig. 3*E1*) showed that, compared with the subsequent spikes, the voltage dynamics of the first spike (red line) were clearly slower in their prepeak phase (dV/dt > 0). Furthermore, we noticed that the AP-threshold of the first AP generated in delayed spiking mode was significantly more depolarized (–42.9 ± 0.49 mV) than that of the next AP generated during the sustained spiking mode (–48.1 ± 0.5 mV) (Fig. 3*E1–2*; $n = 25$). Among all the recorded neuronal classes, the EPSPs of RCan2$^+$ cells were the strongest (2.65 ± 0.15 mV) and more temporally clustered (90.3 ± 15.4 Hz) (Supplementary Fig. 1*B*).

SOM$^+$ Interneurons: Low-Threshold Spiking Properties

SOM$^+$ neurons in the EC tended to orient their dendrites and axons toward the most superficial layers (Fig. 4*A*). The axon of this SOM$^+$ cell appeared thick at the soma and quickly tapered with branching (Fig. 4*A*, inset). More than 80% of the recorded cells in this class showed morphological properties typical of Martinotti interneurons (Tahvildari et al. 2012) as shown in Figures 1 and 4*A*.

Whole-cell recordings in current-clamp configuration were performed on 34 EGFP$^+$ neurons to investigate their electrophysiological responsiveness. SOM$^+$ interneurons exhibited low-threshold-spiking. In terms of passive and active properties, SOM$^+$ cells showed some characteristics that distinguished them from the other subtypes of interneurons (Supplementary Fig. 3). In particular, SOM$^+$ cells showed robust time-dependent inward rectification during injection of hyperpolarizing step currents (SAG ratio = 23.7 ± 1.4%, Fig. 4*B1–2*), which was significantly larger than other cell types recorded (Supplementary Fig. 3*D*), except NPY$^+$ NGF cells and ST cells (see below). In response to hyperpolarizing stimuli (e.g., –230 pA, in Supplementary Fig. 4*A*), SOM$^+$ cells produced I_h-dependent postinhibitory rebound spikes. Spike triggered average (Supplementary Fig. 4*A* inset) revealed two main intrinsic conductances characterizing the period after the spike, a fast-AHP and an afterdepolarization (ADP).

Furthermore, the average AP half-height-width of SOM$^+$ interneurons (0.71 ± 0.02 ms) was significantly wider than RCan2$^+$ interneurons (0.48 ± 0.02 ms) and significantly thinner than those of all other recorded cell types (Supplementary Fig. 3*E*). SOM$^+$ interneurons were weakly adapting (adaptation index = 65.6 ± 1.2%; Fig. 4*C1–2* and Supplementary Fig. 3*G*) compared with the other cell types except RCan2$^+$ cells. Among all the interneurons, SOM$^+$ cells showed the most depolarized resting membrane potential (–70.7 ± 0.5 mV) and a markedly hyperpolarized AP-threshold (–52 ± 1.1 mV), second only to NPY Non-NGF cells (Supplementary Fig. 3*A*). The voltage dynamics of SOM$^+$ APs were quick for the first spike and slowed down with subsequent spikes (Fig. 4*D1–2*). Similarly, the voltage threshold for the first spike (–51.1 mV) was significantly more hyperpolarized compared with voltage threshold of the last spike (–47.2 mV) (Fig. 4*D3*). The use of only two parameters (i.e., adaptation index and AP half-height-width) was sufficient to clearly distinguish RCan2$^+$ and SOM$^+$ cells from each other and from all the other interneuron types (Supplementary Fig. 5).

5HTR3a$^+$ Interneurons: Two Morphological Types, One Intrinsically Variable Cell Class

To characterize passive and active properties of 5HTR3a$^+$ interneurons in the superficial layers of the EC, whole-cell recordings were performed in 42 cells from a mouse line where the 5HTR3a promoter selectively drove the expression of EGFP. 5HTR3a$^+$ interneurons in the superficial layers of the somatosensory cortex were a morphologically and electrophysiologically diverse subclass (Lee et al. 2010). Morphologically, 5HTR3a$^+$ interneurons in LII/III of the EC fell in two subgroups, most of them were bipolar ($n = 28/42$) while the rest were multipolar ($n = 14/42$) (Tahvildari et al. 2012). Dendrites of the bipolar class started thick from a spindle-like soma, and smoothly tapered in both superficial and deeper directions across multiple layers. 5HTR3a$^+$ cells had three to five short and locally branching dendrites. 5HTR3a$^+$ cells showed simpler axonal arborizations compared with either RCan2$^+$ or SOM$^+$ cells but they reached farther in the EC laminae. Despite morphological differences between bipolar and multipolar 5HTR3a$^+$ interneurons, we did not record any significant difference in their active, passive, and firing properties.

Several active and passive properties characterized this subclass of interneurons and distinguished them from the rest. When presented with hyperpolarizing current steps of larger amplitudes, 5HTR3a$^+$ cells showed negligible amounts of time-dependent inward rectification as depicted in Figure 5*C1–2* and Supplementary Figure 3*D* (SAG Ratio = 9.7 ± 0.8%; range 0–20%). Similarly to SOM$^+$ cells, following hyperpolarizing stimuli (e.g., –180 pA, in Supplementary Fig. 4*B*) a few 5HTR3a$^+$ cells could generate postinhibitory rebounds spikes. Spike triggered average of the after-spike voltage responses revealed one characteristic intrinsic conductance, corresponding to a medium-AHP.

More than 95% ($n = 40/42$) of the 5HTR3a$^+$ cells showed substantial spike frequency adaptation (Fig. 5*C3*) that became more evident with stronger depolarizing stimuli (Fig. 5*C4*). Among all the classes recorded, 5HTR3a$^+$ cells were the most adaptive interneuron type (adaptation index = 41.6 ± 2.3%), although the differences with NPY$^+$ NGF and VIP$^+$ cells were not significant. Compared with all the other cell classes, the dV/dt ratio of 5HTR3a$^+$ cells was significantly less negative (–0.27 ± 0.01%).

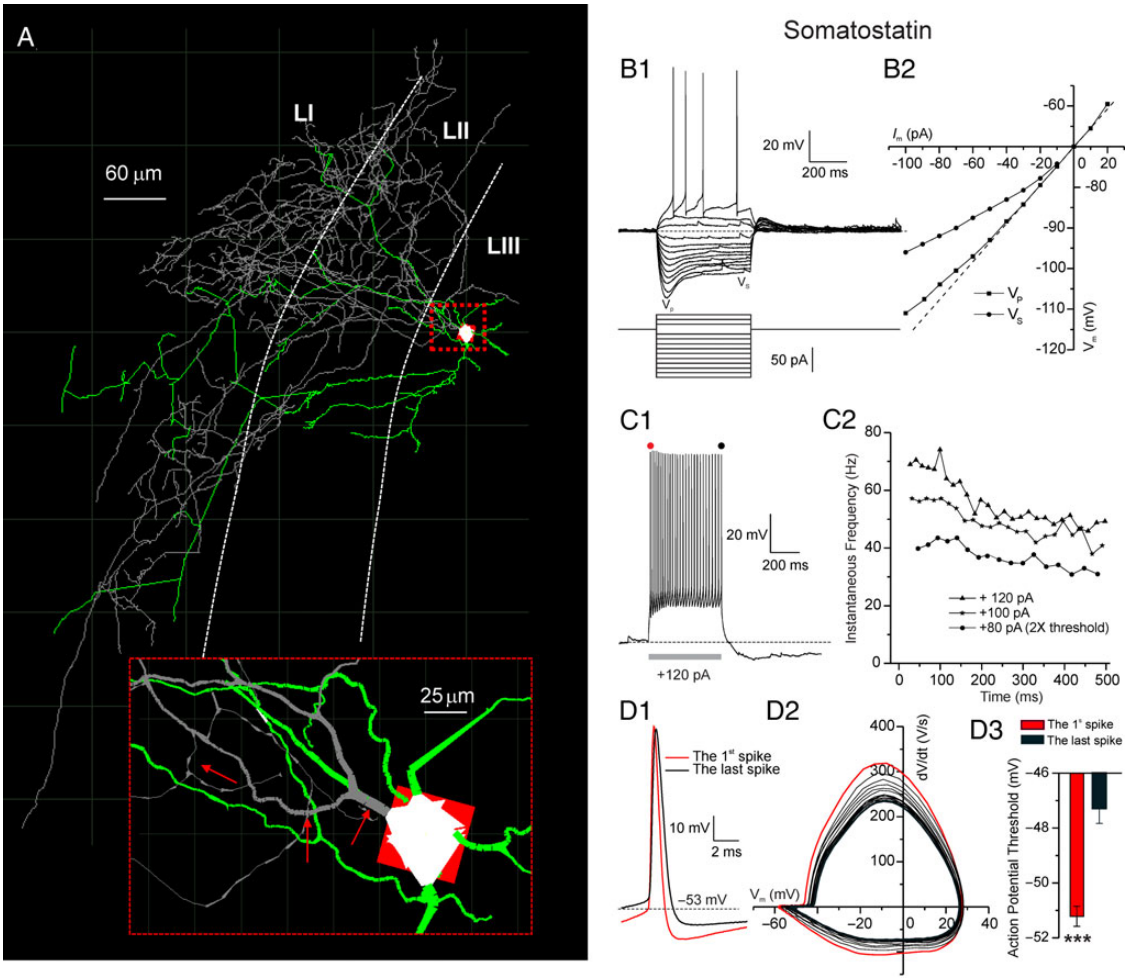

Figure 4. Intrinsic properties of SOM$^+$ interneurons. (*A*) Neuronal 3D reconstruction of an EC SOM$^+$ (GIN) interneuron with dendrites (in green), soma (in white), and axon (in gray). Insets show fine morphological details (e.g., tapering axon, as highlighted by red arrows). (*B1*) Voltage responses to a series of hyperpolarizing and then depolarizing current pulses up to rheobase, with defined voltage-SAG-peak (V_p) and voltage-steady-state (V_s). (*B2*) Current–voltage (*I–V*) relations for each voltage response in *B1* with V_p (squares symbols) and V_s (circles symbols) depicted as two distinct lines. (*C1*) Characteristic voltage response of a SOM$^+$ cell to 120 pA current stimulation with red and black dots highlighting the first and last spike, respectively. (*C2*) Time course of the spike-frequency adaptation for 3 examples of input currents, showing a slow frequency accommodation that depends on the stimulus amplitude. (*D1*) Magnification of the first and last AP, shows that the last AP is has a more depolarized threshold and is slower. (*D2*) Phase plot of somatic spikes show that the changes observed in (*D1*) are gradual as the number of spikes progresses. (*D3*) Significant difference in the voltage threshold for the first and last AP.

Voltage traces (Fig. 5*C5*) and the phase plot (Fig. 5*C6*) of first and subsequent spikes highlighted their kinetic differences, that is, subsequent spikes become slower/wider.

A pharmacological agent was applied to investigate the functional role of the activation of the 5HT3a receptor in modulating the intrinsic properties of these neurons. 1-(m-Chlorophenyl)-biguanide (mCPBG, 100 mM, 50 ms), a potent 5HTR3a agonist, was applied with pressure pulse application in our bath solution while recording electrogenic responses. All three of the 5HTR3a$^+$ interneurons tested responded with high frequency spiking (Fig. 5*D1*) that in 300 ms adapted from ~350 to <100 Hz and persisted for ~10 s (Fig. 5*D2*). This pharmacological response was not observed in any of the NPY$^+$ (NGF or Non-NGF) cells tested (Fig. 5*D1* bottom). This is unlike in somatosensory cortex, where NPY$^+$ NGF cells in the superficial layer do express 5HTR3a (Lee et al. 2010). Analysis of the AP voltage traces (Fig. 5*D3*) showed that the average duration of the AP did not change during the mCPBG puff but the base line voltage became substantially more depolarized (from –52 mV for the first AP to –39 mV in the moment of maximum activation shown in green). Interestingly, the phase plot showing the dynamic evolution of the voltage when mCPBG was applied clearly highlighted that the amplitude of the AP and their speed collapsed at the moment of mCPBG saturation (green line in Fig. 5*D4*) and then went back to normal values as time progressed and the drug washed off (black line in Fig. 5*D4*). 5HTR3a, NPY NGF, VIP, and PYR cells exhibited the smallest EPSPs (1 mV or less) of all cell classes, ~40% the amplitude of the EPSPs received by RCan2$^+$ cells (2.65 mV).

NPY$^+$ Interneurons: Two Electrophysiologically and Morphologically Distinct Groups

We recorded the basic set of intrinsic properties from a subpopulation of NPY$^+$ interneurons ($n = 33$) expressing EGFP. Based on the morphological differences we subdivided the recorded NPY$^+$ cells into two distinct groups (Fig. 6*A*,*B1–2*), NGF ($n = 24$) and Non-NGF ($n = 9$). Always more than four primary dendrites were found branching from the somas of the NGF cells that were generally round and button-shaped. The dendrites of the NGF interneurons were typically restricted to the same layer where the soma

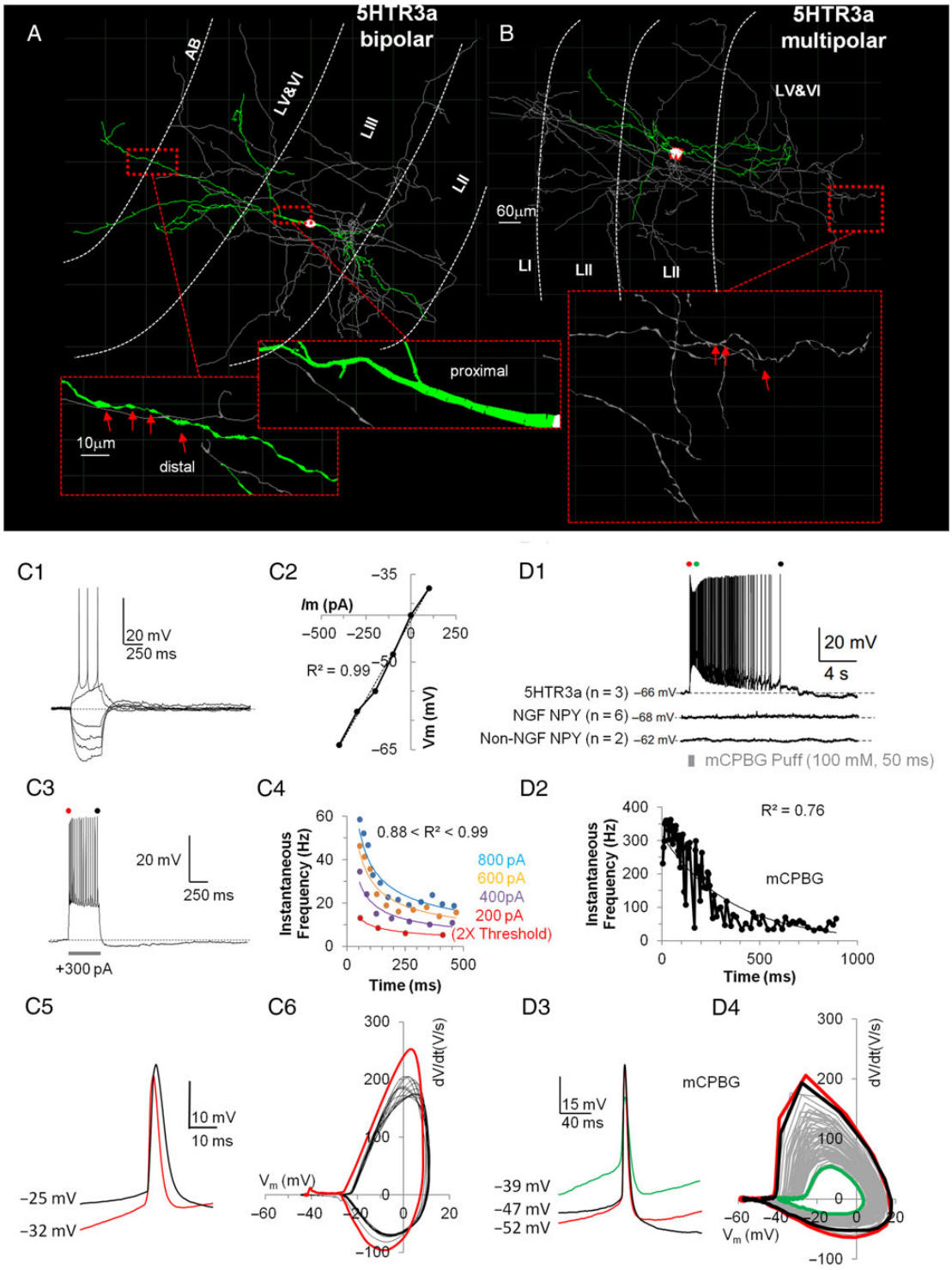

Figure 5. Intrinsic properties of 5HTR3a$^+$ interneurons. (*A*) Computer-aided reconstruction of dendrites (in green), soma (in white), and axon (in gray) of an EC 5HTR3a$^+$ interneuron with bipolar morphology. Insets show fine morphological details (i.e., thick proximal dendrites that taper smoothly, and thin distal dendrites that show pronounced varicosity as highlighted by red arrows). (*B*) Morphology of a multipolar EC 5HTR3a$^+$ interneuron. Insets show fine morphological details (i.e., distinct axonal varicosity, possibly indicative of synaptic boutons). (*C1*) Voltage responses to a series of hyperpolarizing and then depolarizing current steps up to rheobase. (*C2*) Current–voltage (*I–V*) relations for each voltage response in *C1* show no inward rectification. (*C3*) Voltage response at higher current (+300 pA) stimulation, red and black dots show first and last spike, respectively. (*C4*) Time course of the spike-frequency adaptation for 4 amplitudes of depolarizing input currents. Fitting lines are power fits. (*C5*) Superimposed voltage trace for the first (in red) and last spike (in black) to highlight different duration and AP-threshold. (*C6*) Phase plot of the subsequent spikes (in black) shows that adaptation does not affect the shape of subsequent spikes, only the first spike (in red) shows kinetic differences. (*D1*) Characteristic spiking voltage response of a 5HTR3a$^+$ cell to a puff (100 mM, 50 ms) of mCPBG. Note that both classes of NPY neurons do not respond to mCPBG. (*D2*) Exponentially decaying (see mathematical fit) spike frequency adaptation when NPY$^+$ cell is exposed to mCPBG, compare this with the power fits in (*C4*). (*D3*). Superimposed voltage traces for the first (in red), intermediate (in green), and last (in black) spike to highlight same AP duration but different AP-threshold and voltage steady-state after spike. (*D4*) Phase plot of subsequent spikes during mCPBG shows a progression in the spike kinetic shape (gray) that returns to normal (black) after saturating with the green trace.

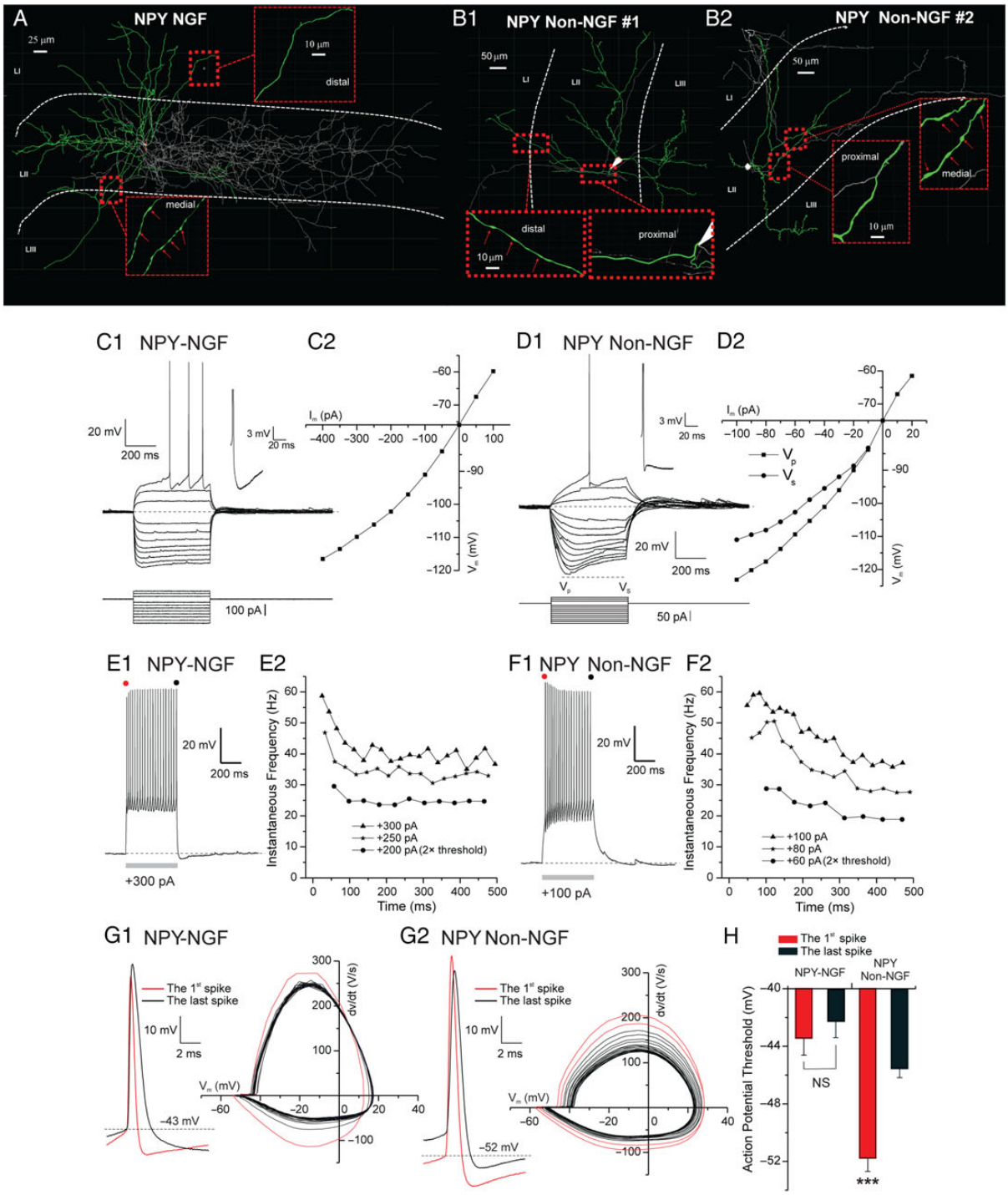

Figure 6. Intrinsic properties of NPY$^+$ interneurons. (*A1*) Computer-aided 3D reconstruction of a NPY$^+$–NGF interneuron color coded for soma (in white), dendrites (in green), and axon (in gray). (*A2*) Same as A1 but for a different NPY$^+$-NGF cell. (*B*) Same as *A1–2* but for a NPY$^+$ Non-NGF cell. (*C1*) Examples of NPY–NGF cell voltage responses to hyperpolarizing and then depolarizing current steps up to rheobase, note minimal SAG response. Inset shows voltage magnification depicting a monophasic fAHP and sAHP current. (*C2*) Plot shows the steady-state voltage response (V_S) to hyperpolarized current steps of different amplitudes (I_m). *D1* Examples of NPY$^+$ Non-NGF cell voltage responses to hyperpolarizing and depolarizing current steps of different amplitudes. Note large SAG response, shown by the difference between voltage peak (V_p) and voltage steady-state (V_s). Inset shows voltage magnification depicting a fAHP current followed by a depolarizing after-potential current (DAP). (*D2*) Plot shows the voltage response to hyperpolarized current steps of different amplitudes (I_m). The two lines represent voltage peak (V_p) and voltage steady-state (V_s), as in (*D1*). (*E1*) Example of NPY-NGF cell spiking response to a suprathreshold current stimulation (+300 pA) lasting 500 ms. (*E2*) Plot showing the time course of the instantaneous firing frequency adaptation for 3 current stimulations of different amplitudes (200, 250, and 300 pA). Note quick spike frequency adaption. (*F1*) Example of NPY–Non-NGF cell spiking response to a suprathreshold current stimulation (+100 pA) lasting 500 ms. (*F2*) Plot showing the time course of the instantaneous firing frequency adaptation for the 3 current stimulations of different amplitudes (60, 80, and 100 pA). Note slower time course of spike frequency adaption compared with (*E2*). (*G1*) Voltage traces (left) and phase plot (right) of somatic spikes show that the fist spike (in red) is quicker that the last (in black) and other spikes. (*G2*) Voltage traces (left) and phase plot (right) of somatic spikes show a gradual progression from the first spike (in red) that is quicker to the last (in black) that is slower. (*H*) Significant difference in AP-threshold for the first and the last spike of NPY$^+$ Non-NGF cell but not for NPY$^+$ NGF.

was located; however, occasionally dendrites penetrated the other layers. In contrast, somas of Non-NGF cells were polygonally shaped and gave rise to 3–4 primary dendrites spanning across multiple layers. In Non-NGF interneurons, the axon developed into extremely focal and densely intertwined arborizations of ultrathin structures with several orders of branching. Compared with their dendrites, extending radially ~250 μm from the soma in Euclidian distance, the axons of these interneurons covered a greater extent of the entorhinal cortical field, ~600 μm from the soma. On the other hand, NGF interneurons possessed less dense and branched axons but they spanned multiple layers.

We found that, according to a series of passive and active membrane properties, there were significant differences between NGF and Non-NGF NPY$^+$ interneurons as well as between NPY$^+$ interneurons and the other cell classes (Supplementary Fig. 3 and Table 2). Input resistance, membrane time constant, and AP amplitude (Supplementary Fig. 3*B*, *C*,*I*, respectively) were significantly smaller in NGF compared with Non-NGF interneurons. In addition, NGF cells had a significantly more depolarized AP-threshold than Non-NGF interneurons (Supplementary Fig. 3*F*). With respect to other spike characteristics, the APs of the NGF neurons were always followed by a monophasic fAHP and sAHP (inset in Fig. 6*C1*). fAHP conductances regulate the AP half-width and thus Ca^{++} influx during depolarization. In contrast, the APs of Non-NGF neurons in most cases (7 out of 9) had a fAHP followed by a depolarizing after-potential current (DAP) (inset in Fig. 6*D1*). Analysis of the current/voltage (*I*/*V*) relationships demonstrated that NGF neurons manifested only a small amount of time-dependent inward rectification (Fig. 6*C1–2*) (SAG ratio = 6.9 ± 0.6%) that was much more prominent (SAG ratio = 24.1 ± 2.1%) in Non-NGF neurons (Fig. 6*D1–2*). Both NGF and Non-NGF interneurons displayed marked inward-rectification in the hyperpolarizing direction as reflected by the upward bending of the I/V curve toward the negative end (Fig. 6*C2*,*D2*). As for SOM$^+$ cells and for some 5HTR3a$^+$ cells, hyperpolarizing currents (e.g., –200 pA in Supplementary Fig. 4*C*) could generate postinhibitory rebound spikes in NPY$^+$ Non-NGF neurons. Unlike SOM$^+$ and 5HTR3a$^+$ neurons, the spike triggered average in NPY$^+$ Non-NGF cells (Supplementary Fig. 4*C* inset) revealed no intrinsic conductance dominating the after-spike voltage response.

As in RCan2$^+$ cells, one of the most noticeable features of NGF interneurons was the ability to generate spikes with a prominent delay during peri-AP-threshold stimulations (Fig. 6*C1*). Such behavior was less present in Non-NGF interneurons. We analyzed the input–output relationship of these interneurons by stimulating them with depolarizing current steps. This analysis revealed two significant differences between the NGF and Non-NGF cells. First, in response to the high-amplitude current step pulses, the NGF cells always reacted with a fast-adapting discharge followed by a highly regular tonic phase (Adaptation index 42.6 ± 1.9%, Fig. 6*E2*). In contrast, the spiking behavior of Non-NGF cells was less adapting and showed adaptation with a slower time course (Adaptation index 54.7 ± 4.1%, Fig. 6*F2*). In other words, the firing rate of NGF interneurons during high-amplitude current stimuli swiftly adapted (in 150 ms) and then was maintained while Non-NGF interneurons continued to slowly accommodate over a period of 500 ms. The phase plot analysis (dV/dt vs. V_m) revealed that spike amplitude, spike threshold, and maximum slope was constantly maintained almost among all the APs generated during high-amplitude stimuli in NGF interneurons. On the other hand, the majority of the Non-NGF cells (7 out of 9) showed a spiking pattern characteristic of the low-threshold spiking interneurons. Moreover, the phase plot analysis of the APs in the Non-NGF cells exhibited a gradual shift of the AP threshold, AP amplitude attenuation, and also attenuation in the net outward current during step depolarizing current pulses of high amplitude (Fig. 6*G2*, right panels). The AP-thresholds for the first and last spikes were significantly different in Non-NGF but not in NGF interneurons (Fig. 6*H*). Compared with all the other cell classes, the amplitude of the EPSPs during Up states in NPY$^+$ Non-NGF cells (1.81 mV) was second only to RCan2$^+$ cells (2.65 mV). Similarly, the frequency of the EPSPs in NPY NGF cells (59.4) was the highest of all cell classes, except for the RCan2$^+$ cells (90 Hz) (Supplementary Fig. 1*B*).

VIP$^+$ Cells: Two Functional Groups Based on Their Firing Properties

We recorded the membrane voltage dynamics of 19 VIP$^+$ interneurons expressing Zs-green in LII/III of the EC. Sixteen of the nineteen VIP$^+$ interneurons had a bipolar/double-bouquet morphology with basal dendrites branching perisomatically (in LII/III) and one (or two) main dendritic trunk(s) projecting to the most superficial layers of the EC (LI/II) and further branching along the way (Fig. 7*A*). Axons of VIP$^+$ cells stemmed off basally from a spindle-shaped soma and, typically of double-bouquet cells (Kawaguchi and Kubota 1997), branched extensively in intertwined arborizations protruding into the deeper layers of the EC.

Hyperpolarizing current stimulations revealed that VIP$^+$ interneurons were characterized by minimal time-dependent inward rectification (SAG ratio = 8.8 ± 1.2%, Fig. 7*B1–2*) which became noticeable only with stronger hyperpolarizing stimuli (Fig. 7*B1–2*). As previously reported (Tahvildari et al. 2012), when presented with depolarizing step current stimuli, 73% of the VIP$^+$ interneurons showed classical adaptive-regular spiking. Interestingly, the remaining 27% of VIP cells produced irregular spiking and some of these cells increased/accelerated their firing frequency before reaching a plateau in later spikes (Fig. 7*C1–2*,*D1*); some of the RCan2$^+$ cells also manifested this phenotype. The AP voltage dynamics of this second group of VIP$^+$ cells started by quickly accelerating, then became slower after each AP (Fig. 7*D2*) despite the fact that AP frequency was increasing over time. Also, in these cells larger depolarizing stimulations (>400 pA) led to the activation of a slow AHP conductance that was mostly absent when the stimulations were peri-AP-threshold (Fig. 7*C1–2*).

Compared with all the other cell classes (Table 1) VIP$^+$ interneurons stood out in several respects; they had the highest input resistance (508 ± 43 MΩ), the lowest AP amplitude (59.5 ± 1.2 mV), and the longest AP half-height-width (1.19 ± 0.04 ms). Furthermore, the APs of VIP$^+$ cells were among the most adapting (42.7 ± 1.5%), with a highly depolarized thresholds (–44.3 ± 0.5 mV) that was second only to NPY$^+$ NGF cells (–43.5 ± 0.6 mV). They also had the slowest membrane time constants (38.5 ± 2.6 ms) except for SOM$^+$ cells (39.6 ± 3.7 ms).

f-I Curves and Recruitment of Individual EC Cell Populations

So far we analyzed intrinsic properties at the single cell level but it would be useful to see how different cell populations functionally relate to each other. We used sigmoidal functions (Fig. 8*A* top, blue line) to describe the relationship between input currents and the output firing rates (*I*/*O*) of single cells. Significant differences in the *I*/*O* curves of neurons from the same cell class emerged from this type analysis (Fig. 8*A* top, gray sigmoids). The sigmoids of each neuronal population (Fig. 8*A* top) can then be averaged to produce an average firing rate (Fig. 8*A* bottom). These results show that VIP cell population produce the lowest maximal firing rate in the EC (34 Hz when a 600 pA current step was applied)

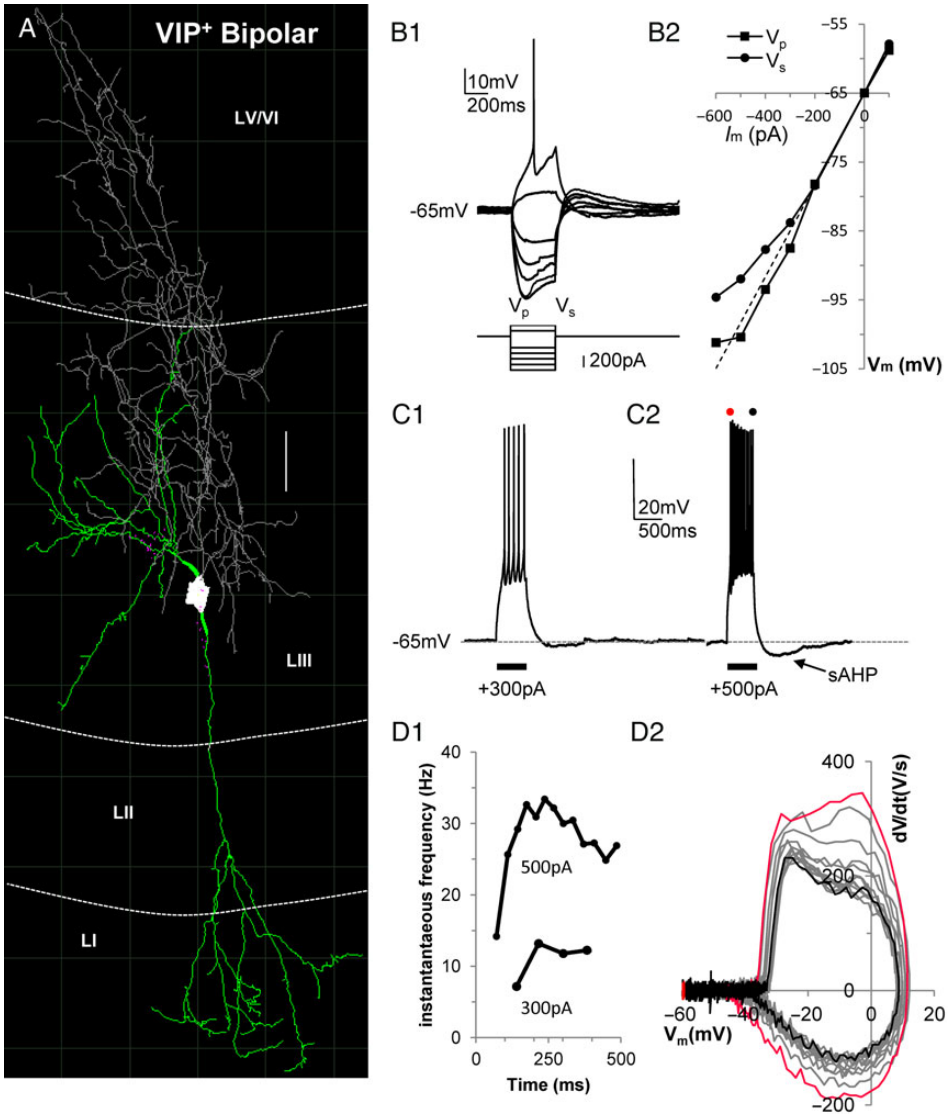

Figure 7. Intrinsic properties of VIP+ interneurons. (*A*) Computer-aided 3D reconstruction of a VIP+ interneuron color coded for soma (in white), dendrites (in green), and axon (in gray) (scale bar = 25 μm). (*B1*) Voltage responses to a series of hyperpolarizing and then depolarizing current pulses up to rheobase. Note the large SAG response, shown by the difference between voltage peak (V_p) and voltage steady-state (V_s). (*B2*) Plot shows the voltage response (V_m) to hyperpolarized current steps of different amplitudes (I_m). The two lines represent voltage peak (V_p) and voltage steady-state (V_s). (*C1–2*) Example of VIP cell spiking response to 2 suprathreshold current stimulations (+300 and +500 pA) lasting 500 ms each. Note the sAHP component emerging after strong depolarizing stimuli. (*D1*) Plot showing the time course of the instantaneous firing frequency adaptation for the 2 current step stimulations shown in *C1–2*. (*D2*) Phase plot of subsequent spikes shows that as the instantaneous firing frequency increases the spike themselves become slower (compare red and black line for first and last spike, respectively).

while, RCan2 neurons were the fastest cells, able to fire at a frequency that was 4.5 times higher than VIP+ cells (154 Hz) given the same amount of current (600 pA). We define a single cell as being recruited when for a given input current the cell reaches 50% of its maximal firing rate. The cumulative distribution of each cell recruited in each neuronal class is the activation curve for that specific cell class (Fig. 8A top, in red). We plotted the activation curves for each EC neuronal population studied (Fig. 8B).

Intrinsic Properties Identify Functional Clusters of EC Neurons

Whole-cell recordings from EC interneurons showed a marked heterogeneity between and within distinct cell classes with wide variation in their intrinsic properties. We were interested in functionally segregating cell types based on their physiological properties. To achieve this we produced pair-wise scatter plots for the active properties of interneurons and color-coded the data by cell type (Supplementary Fig. 5). RCan2+, SOM+, and VIP+ cells appeared almost completely separable from each other solely on the basis of AP half-height-width and adaptation index. Correlation values (Pearson's *r*) for all pairs of features are shown on the right side of the correlation matrix (in Supplementary Fig. 5). Some features are highly correlated. For example, AP half-height-width explained nearly half the variance in Adaptation Index. Similarly, AP-threshold explained 40% of the variance in the AP-amplitude (this may be expected since we used the value of the AP-threshold to calculate the AP-amplitude). This analysis suggests that some intrinsic features may provide little, if any, new information, when classifying neurons based on their function.

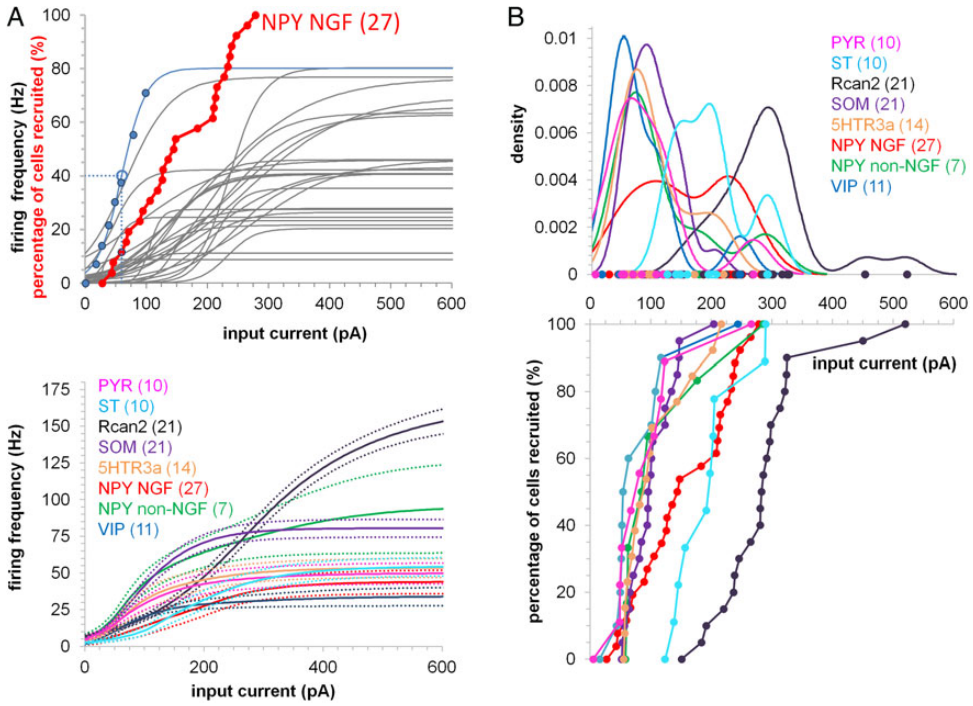

Figure 8. *f–I* curves and recruitment of distinct cell populations. (*A*) Top, Blue data points represent the firing frequency against input current for one NPY NGF cell (blue line is a sigmoid fit). Dashed lines indicate 50% of the cellular maximal estimated firing frequency (i.e., the value for which a cell is considered recruited). Red data points represent the activation curve of the NPY NGF cell population (that is, the cumulative distribution of input currents eliciting 50% firing frequency, $n = 27$). The red data point with the blue border is the cell with the blue sigmoid fit. Gray sigmoid fits indicate the firing frequency of the 27 NPY NGF cells making up the activation curve. Bottom, average firing frequency (solid lines) and standard error (dotted lines) for each EC cell population (calculated averaging the sigmoid fits of each cell). (*B*) Bottom, activation curves for each neuronal population as function the input current. Top, density estimation of the probability to recruit each neuronal population with a specific input current. Bimodality suggests distinct functional subpopulations within a cell class.

To identify the source of such variability better, we performed 9D unsupervised cluster analysis (Ward 1963) on the passive and active intrinsic properties recorded from each EC cell. This analysis allowed us to segregate groups of EC neurons with similar properties and identify functionally distinct subgroups within the same neuronal class. We identified 7 clusters of EC neurons (clusters A–G; Fig. 9A). The principal cells in EC (ST and PYR) produced isolated clusters that were functionally close to each other. Their intrinsic properties fell in the middle of all the interneuron classes, whose properties were much more diverse. RCan2$^+$ cells also produced a well-separated cluster that functionally fell on the opposite side from most of the NPY$^+$–NGF cells. Interestingly, SOM$^+$ cells formed two functionally distinct subgroups. One of these subgroups (B, included 76% of SOM$^+$ cells) was intrinsically more similar (based off the Euclidian distance) to most NPY$^+$–Non-NGF cells than to the other SOM$^+$ subgroup (C). 5HTR3a$^+$ interneurons were the most heterogeneous group, with ~66% of them being functionally related to most VIP$^+$ cells (16 out of 19), ~15% of them being closely related to SOM$^+$ cells and to NPY$^+$ Non-NGF cells, and ~13% of them functioning more like NPY$^+$–NGF interneurons.

Using a complex multidimensional model to understand cell function is useful but we were interested in extracting the most salient intrinsic features that allowed us to classify neurons with a good level of accuracy. To achieve this goal we reduced the multidimensional space of intrinsic properties to the most salient five (i.e., adaptation index, SAG, dV/dt, membrane time constant, and AP-threshold) that predicted with high accuracy the cellular biomolecular identity based on their intrinsic properties. This analysis can be visualized as a decision tree (Breiman et al. 1984) that can be traversed to its terminal nodes (functional cell classes) based on thresholds for intrinsic properties. In short, we derived the classifying criteria that led to the production of similar functional clusters as the ones in Figure 9A using only 5 intrinsic parameters rather than 9. For example, Cluster A in Figure 9A mostly corresponded to Node 3 in Figure 9B, in including mostly RCan2$^+$ cells; Cluster D mostly overlapped with Node 11 comprising mostly PYR cells; Cluster E corresponded to Node 9 encompassing most ST cells; Cluster F as Node 15 included 5HTR3a$^+$ and VIP$^+$ cells; Cluster G and Node 6 were mostly composed of NPY$^+$ NGF cells; and finally, Clusters B and C corresponded to Nodes 12, 13, and 14 being made of a mix of SOM$^+$, NPY$^+$ Non-NGF, 5HTR3a$^+$ cells. These five parameters represented the most efficient predictors of EC interneurons functional grouping based on a supervised clustering method. As a brief example, on its own an adaptation index larger than 0.79 was able to discriminate 90% of the RCan2$^+$ cells. While, for the remaining cells (with adaptation index <0.79) if their SAG ratios were larger than 15.5% and their dV/dt ratios were larger than −0.28%, there was a 93% chance that they were ST cells. In short, fully traversing the tree in Figure 9B1 allowed total cell classification based on conditional statements regarding their five intrinsic properties. Complementary to the bar graphs in Figure 9B1,B2 showed how many neurons of each cell class ended up in each terminal node, suggesting minimal functional overlap between different cell classes.

This analysis (Fig. 9B1–2) suggested that 5 parameters were sufficient to separate EC cells into the 8 functional clusters. To understand the importance of each of the original 9 intrinsic parameters, we removed them, 1 at the time, from our analysis

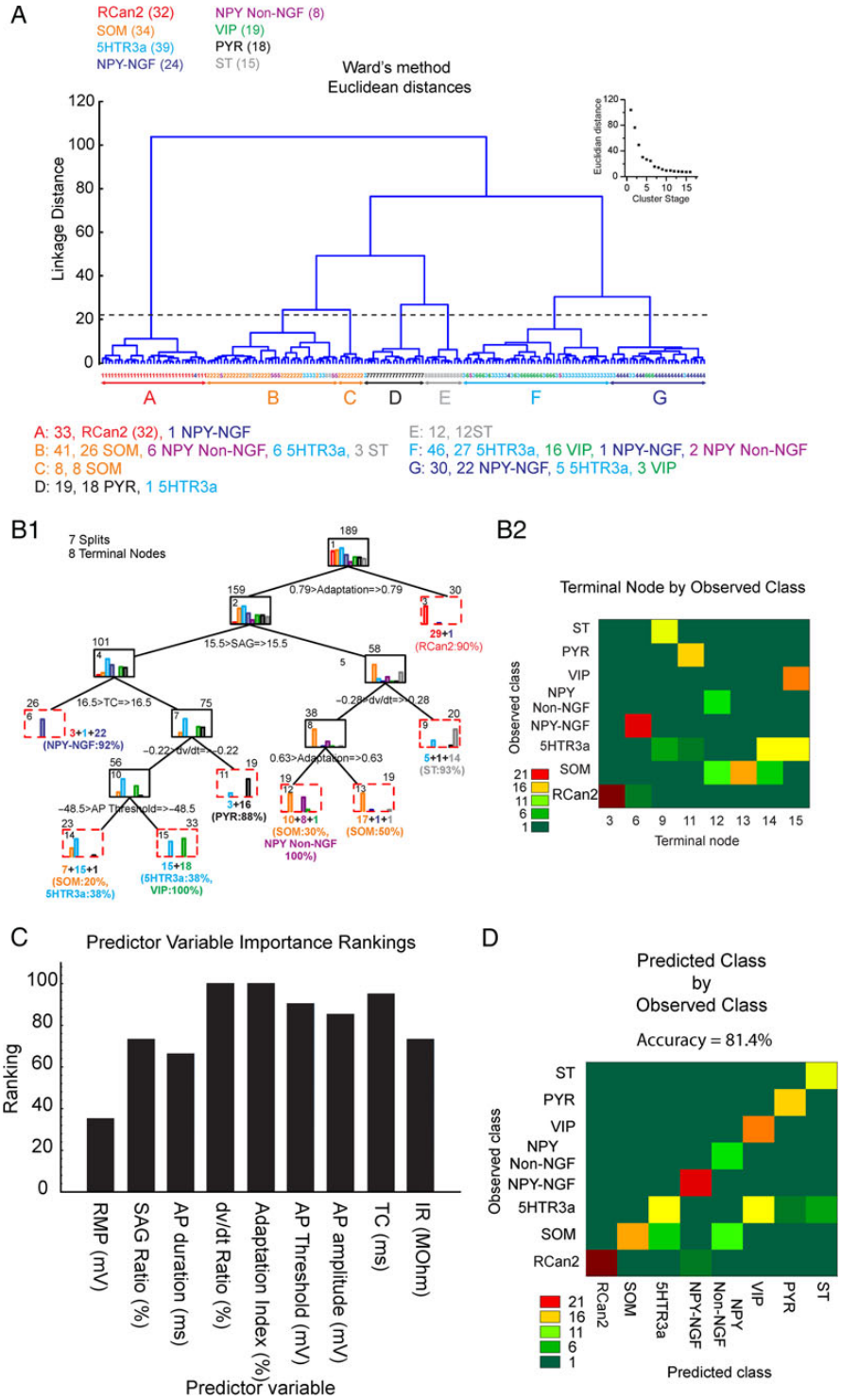

Figure 9. Intrinsic properties of neurons in layers II/III of mouse EC identify 7 subgroups of cells. (*A*) Unsupervised method of cluster analysis. Dendrogram derived from a 9D-cluster analysis (based on the 9 intrinsic properties) using Ward's method with a Euclidean distance measure to functionally classify 189 patched interneurons. Dendrogram intersections with the *x*-axis represent individual cells while average linkage distance between neurons is represented on the *y*-axis, where larger linkage distance represents larger dissimilarity. Cutoff (horizontal dashed line) defines seven primary clusters, with colored letters at the bottom defining their boundaries. Inset shows the clustering amalgamation schedule, indicating linkage distances at successive clustering steps. A shallower slope after the formation of cluster # 7 validates the cutoff point. (*B1*) Supervised method of cluster analysis. Decision tree analysis shows that clusters formed with the 9D analysis in A and represented by different colored bars in (*B1*), can be closely reproduced with only 5 parameters (Adaptation; SAG; time constant; dV/dt; and AP-threshold). Numbers on top of each box indicate the total number of neurons in that branch, while numbers at the bottom of the boxes indicate the number of neurons in each color-coded bar graph. Numbers inside boxes indicate the number of the node. (*B2*) Heat map depicting the number of neurons for each cell class (*y*-axis) that ends up in terminal node in (*B1*). (*C*) Ranking of the importance of each intrinsic property (predictor variables) to the prediction made by the cluster analysis. RMP, resting membrane potential; TC, time constant; IR, input resistance. (*D*) Model accuracy calculated as percent neurons correctly classified (on the diagonal) and misclassified (off of the diagonal).

and ranked them by predictive importance (in Fig. 9C). The two most salient parameters were the dV/dt ratio and the Adaptation Index while the two weakest predictors were the resting membrane potential and the AP-duration. Finally, to understand how well intrinsic properties predicted the observed class we showed that the identity of 81.4% of cells was accurately predicted using only our 9D model (Fig. 9D). Based on the decision tree analysis, RCan2$^+$, ST, and NPY$^+$–NGF are easiest cells to classify (only requiring 1 and 3 parameters, respectively) while SOM and 5HTR3a, were the most difficult to separate (requiring 4 and 5 parameters, respectively). Ideally, a higher accuracy could be achieved by including more intrinsic properties for the specific cell class of interest.

Discussion

The cell classes investigated in this study may be grid cells or play an important role in modulating grid cell function. One of the outstanding challenges for future neurophysiologists will be characterizing the neuronal circuitry in the brain that codes spatial location (i.e., place cells in the hippocampus and grid cells in the EC) (Giocomo et al. 2011a, 2011b; Buzsaki and Moser 2013; Craig and McBain 2015; Hasselmo and Stern 2015). In this study, we used genetically fluorescent cell lines to identify and record electrophysiological, morphological, and neurochemical data from different cell types in the superficial layers of the EC. Unfortunately, unlike in the hippocampus (Bezaire and Soltesz 2013), we know very little about how these cells are connected to each other in the EC.

As we previously discussed, there is not much intracellular data on EC interneurons, so our whole-cell recordings (Figs 2–8 and Supplementary Fig. 3) can primarily be compared with the consistent neuronal classes in superficial cortical layers of other brain regions. Our results in the EC seem consistent with previously reported data on O-LM SOM$^+$ interneurons in the hippocampus (Chittajallu et al. 2013), where the majority of SOM$^+$ cells show slowly accommodating APs, high input resistance, slow membrane time constants, and large SAG responses upon hyperpolarization. As in LII/III of the barrel cortex (Lee et al. 2010), our 5HTR3a$^+$ neurons exhibited high-input resistance. But unlike barrel cortex cells, EC 5HTR3a$^+$ cells rested at more hyperpolarized membrane potentials (~−60 and ~−70 mV for barrel cortex and EC, respectively) and exhibited slower membrane time constants (~30 ms) compared with those in the barrel cortex (~20 ms). Similarly to Lee et al. (2010), our 5HTR3a$^+$ cells quickly depolarized when serotoninergic receptors were activated (i.e., when we pharmacologically activated them with mCPBG). As in our study, NPY$^+$ interneurons in the striatum can also be divided in NGF and Non-NGF (Ibáñez-Sandoval et al. 2011) but striatum interneurons possess substantially less I_h (i.e., smaller SAG responses upon hyperpolarization) than their EC counterparts. On the other hand, in the neocortex Karagiannis et al. (2009) found three subtypes of NPY$^+$ interneurons: a superficial NGF-like cell, with dense axonal arborizations that coexpress nitric oxide synthase; a FS basket cell-like cell coexpressing PV, with pronounced spike latency; and an easily excitable Martinotti-like cell coexpressing SOM with ascending axon ramifying into LI. Interestingly, this last group of NPY$^+$ cells is consistent with our result suggesting that some SOM$^+$ and NPY$^+$ Non-NGF might functionally overlap (see Fig. 9A Cluster B&C and Fig. 9B1Nodes 12, 13, 14). Historically, VIP$^+$ interneurons have been considered the controllers of metabolic energy expenditures in cortical function (Magistretti and Morrison 1988) but work from Connor and Peters (1984) and Hajós et al. (1988) demonstrated that these cells are also embedded in complex cortical circuitries, receiving both excitatory and inhibitory synaptic inputs and delivering inhibitory synaptic outputs. Other groups (Kawaguchi and Kubota 1996; Cauli et al. 1997) have characterized the intrinsic properties of VIP$^+$ cells in the prefrontal cortex of the rats. A comparison with these datasets suggests that VIP$^+$ cells in the EC of the mouse tend to have resting potentials that are more hyperpolarized (~−71 mV) compared with VIP$^+$ cells in the prefrontal cortex (−66 mV) of the rats. Furthermore, EC VIP$^+$ cells spike widths are also 43% longer (1.1 ms) compared with VIP$^+$ cells in the prefrontal cortex (0.77 ms). Our study also suggests that VIP$^+$ cells in EC have a much higher input resistance (508 ± 43 MΩ) than VIP$^+$ cells in other superficial cortical areas (327 ± 83 MΩ) (Porter et al. 1998).

It is also possible that some of the reported differences in intrinsic properties between classes of interneurons in the EC and in other brain regions could be due to age differences in the animals. Some intrinsic (ion channels) and extrinsic (synaptic) features are indeed age-dependent and undergo a significant maturation process that may affect cellular function (Johnson and Felder 1993). It is also important to highlight that our electrophysiological recordings are performed at 32°C. All ion channels are temperature-sensitive (Moran et al. 2004). For instance, the TRP channel (Caterina et al. 1997; Clapham 2003; Patapoutian et al. 2003; McKemy et al. 2002), the TMEM16A channel (Cho et al. 2012), the voltage-gated H$^+$ current (DeCoursey and Cherny 1998), the hERG channel (Vandenberg et al. 2006), the TREK1 channel (Maingret et al. 2000), the ClC-0 channel (Pusch et al. 1997), and the voltage-gated sodium channel (Dib-Hajj et al. 2008) are all known to be strongly modulated by changes in temperature. These studies suggest a molecular framework for temperature-dependent gating of ion channels (Chowdhury et al. 2014). Therefore, characterization of intrinsic excitability ought to be conducted and compared at near physiological temperatures.

Overall we showed that each class of principal cells and interneurons in the superficial EC is endowed with a diverse set of intrinsic properties that make them unique. Our data also suggest that some classes of cells show remarkable variability (5HTR3a$^+$ and SOM$^+$ cells) while other (RCan2$^+$, PYR, and ST cells) are more functionally homogeneous. In considering the ability of intrinsic properties to separate interneuron types in EC, it is clear from the cluster analysis that some groups of interneurons more strongly differ in their intrinsic properties (e.g., RCan2$^+$ cells) and therefore lie in distant regions of the multidimensional space of intrinsic properties. Also, some cell types are functionally closer (e.g., PYR and ST). This is most readily seen by observing the linkage distances resulting from each cluster stage and noting that, as more clusters are created the change in Euclidean distance resulting from the new cluster is often smaller. However, it is important to note that cell types (i.e., clusters) with small difference in their intrinsic properties, are still often accurately separable. For example, although PYR and ST cells are very similar, they can still be distinctly separated with no mixing in intrinsic property space. In any case, we acknowledge that finding a finite set of fixed parameters sufficient to functionally categorize all neuronal types in any brain region is difficult. In reality intrinsic properties of a given EC cell type likely fall within a distribution having tails overlapping with parameter distributions of other cell types. Nevertheless, as intrinsic properties play a large role in shaping cellular activity (and therefore ultimately cell function) we felt that using these parameters to predict cell types was the logical next step in cell classification. Furthermore, although several cell types did not differ greatly

overall in their intrinsic properties, in many cases these types were still cleanly separable in the analysis.

We also provided amplitudes and frequencies of the incoming spontaneous EPSPs for each cell class during up states (Supplementary Fig. 1B), but these values were also extremely variable. We suspect cellular differences in active and passive properties might strongly contribute to this variability (rather than pure differences in synaptic strengths) as this has been previously observed in another cell class in the hippocampus (Perez-Rosello et al. 2011).

These data might assist in understanding specific functional roles for some of these different types of inhibition in EC. For example, our laboratory previously showed a loss of grid cell spatial periodicity in medial EC during inactivation of medial septum inputs (Brandon et al. 2011). Recent data shows that the medial septal input primarily contacts inhibitory interneurons in EC (Gonzales-Sulser et al. 2014). A recent study (Buetfering et al. 2014) showed that PV$^+$ interneurons inhibited all functionally defined cell types in the medial EC and in turn received input from grid cells. In addition, it has been shown that stellate cells in EC interact primarily via FS interneurons (Couey et al. 2013). The synaptic inhibition regulated by medial septum and by other stellate cells could interact with the hyperpolarization-activated cation current (I_h) that gives slow intrinsic resonant properties to cortical neurons (Hutcheon and Yarom 2000) including entorhinal stellate cells (Dickson et al. 2000; Haas and White 2002; Erchova et al. 2004; Giocomo et al. 2007; Giocomo and Hasselmo 2009; Boehlen et al. 2010).

The presence of I_h in some cell types may enable them to produce postinhibitory rebound spikes. Suggesting that when hyperpolarizing currents (such as GABAergic synapses) get turned off, I_h-expressing neurons will experience an overshoot in their membrane potential that may lead to one or more action potentials. Through this mechanism (strong IPSPs and strong I_h conductances), action potentials can be triggered with a certain delay after the arrival of the inhibitory inputs (IPSPs). We have previously shown that SCs (and in a minor capacity PCs) in EC could generate postinhibitory rebound spikes in vitro (Shay et al. 2015; Ferrante et al. 2016) and in vivo (Tsuno et al. 2015; Ferrante et al. 2016). Here (Supplementary Fig. 4) we tested EC interneurons for their ability to produce spikes in response to inhibitory stimuli. Most NPY Non-NGF$^+$ cells and SOM$^+$ cells could produce postinhibitory rebound spikes with ~200 pA hyperpolarizing current pulses. Also, some 5HTR3a$^+$ cells (perhaps expressing more I_h than normal) could also produce postinhibitory rebound spikes. In particular, the I_h current allows stellate cells more than Pyramidal cells to respond to hyperpolarization with postinhibitory rebound spikes both in vitro and in vivo (Alonso and Llinás, 1989; Alonso and Klink 1993; Shay et al. 2015; Tsuno et al. 2015; Ferrante et al. 2016). Based on these data, it has been proposed (Hasselmo 2013; Hasselmo and Shay 2014) that cells that strongly express I_h (such as ST cells, or possibly SOM$^+$ and NPY-Non-NGF cells) could maintain persistent firing even with purely inhibitory synaptic connections generating postinhibitory rebound spikes. These rebound spiking mechanisms could contribute to the mechanism of grid cell firing (Hasselmo 2013; Hasselmo and Shay 2014), including temporal properties of grid cell firing relative to theta rhythm oscillations in the field potential (Hafting et al. 2008; Mizuseki et al. 2009) such as theta phase precession (Hafting et al. 2008; Climer et al. 2013; Eggink et al. 2013) and theta cycle skipping (Brandon et al. 2013). The I_h might also regulate filtering of unsynchronized excitatory inputs on distal branches (Migliore et al. 2004). Other ionic channels (I_{CAN} and BK) have also been shown to contribute to the initiation, termination, and regulation of persistent firing in EC principal cells (Fransén et al. 2006; Tahvildari et al. 2007, 2008). Alternatively, interneurons with little I_h, such as FS cells, may be preferentially involved in supporting higher frequency, e.g., gamma band rhythms (Cardin et al. 2009; Salkoff et al. 2015).

Experimental evidence in other cortical structures suggests that SOM$^+$ (Xu et al. 2013) and PV$^+$ (Hu et al. 2014) cells in LII/III tend to inhibit PYR cells. Functionally, feed-forward inhibitory mechanisms involving SOM$^+$ (bistratified) cells and PV$^+$ (basket) cells enable PYR cells to remain easily excitable while faithfully representing a broad range of excitatory inputs without quickly saturating (Pouille et al. 2009; Ferrante and Ascoli 2015) by buffering, subtracting, or dividing the principal cell input–output (Ferrante et al. 2009; Ferrante and Ascoli 2015). In other cortical structures, the VIP$^+$ subclass selectively inhibits PV$^+$ and SOM$^+$ interneurons (Lee et al. 2013; Pfeffer et al. 2013; Pi et al. 2013; Fu et al. 2014), thereby disinhibiting neocortical PYR cells and possibly grid cells. In other words, while other interneuronal classes are thought to provide an indiscriminate blanket of inhibition to the cells that surround them, holes in this blanket can be generated by VIP$^+$ cells (Karnani et al. 2014). These data suggest a possible model for the emergence of grid cells firing that takes into account interactions of inhibitory interneurons. This network model suggests that PV$^+$ and SOM$^+$ could function as antigrid cells, while the activation of VIP$^+$ interneurons and therefore disinhibition of grid cell firing would be happening during in-field spatial navigation. Interestingly, VIP$^+$ cells are activated by nicotine (Alitto and Dan 2013) and by acetylcholine (Lee et al. 2010) which would suggest a potential mechanism for the influence of cholinergic modulation on grid cell firing (Newman et al. 2014).

As techniques for manipulating specific membrane channels progress, aided by computational methods (Burgess et al. 2007; Ferrante et al. 2008; Burak and Fiete 2009; Giocomo et al. 2011a, 2011b), it would be interesting to selectively target membrane proteins and regulate intrinsic properties in restricted subpopulations of cells to test how they may affect grid cell firing.

Our immunohistochemistry results (Supplementary Fig. 2) did not detect GABA in most RCan2$^+$, 5HTR3a$^+$, and SOM$^+$ cells in the EC. It is important to note that these results did not exclude the possibility that our immunohistochemistry results might be compromised (e.g., the fluorescence of the GABA immunohistochemistry was not easily detectable) as this is indeed a common limitation in immunohistochemistry (Dunstan et al. 2011).

Small differences in neuronal morphologies, for example, the shape of the dendritic branch point (Ferrante et al. 2013) and the diameter ratio between father and daughter branch (Migliore et al. 2005) can have a large impact in cell capacity to integrate, generate, and propagate electrical signals. With this idea in mind and with the purpose of aiding future investigations and analyses, we provided (through NeuroMorpho.org) 3D reconstructions of nine EC cells from all cell classes, except ST cells; as ST reconstructions were already available in the Nolan archive (Garden et al. 2008) in NeuroMorpho.org. These neuronal reconstructions could be used to implement dynamical models that work at different scales and test predictions of neuronal computational properties (Ferrante 2012).

The final set of results presented here (Fig. 9 and Supplementary Fig. 4) provided a framework for classification of functional subtypes of cortical neurons by their intrinsic electrogenic properties. Recent experimental advances, for example, the advent of all-optical electrophysiology (Hochbaum et al. 2014) are accelerating the pace of data collection by enabling researchers to optically stimulate and record voltage traces from several neurons simultaneously. This rapid growth of information about

physiological, morphological, and molecular properties of neurons requires automating the methods for neuronal classification by using powerful machine learning techniques (Armañanzas and Ascoli 2015). Other studies inspired this manuscript by using supervised and unsupervised cluster analysis methods to segregate neurons based on their morphological (Guerra et al. 2011) or their functional and physiological (Krimer et al. 2005; Sosulina et al. 2006; Hadzipasic et al. 2014; Keshavarzi et al. 2014) properties. In these previous attempts the neuronal identity was often not clear or was limited to one or few cell classes. This method showed how well the results of cluster analysis of intrinsic properties compare with segregation of cells by specific biomarkers. On the other hand, our approach aims to provide a genetically validated framework for neuronal functional classification that could predict 81.4% of the molecular cell classes based on the intrinsic properties. The accuracy of this clustering method may vary when used in other brain regions, cell classes, or with a different set of intrinsic properties; for this reason, it would be interesting to test how our results compare in other conditions.

Authors' Contributions

M.F. and B.T. wrote the paper with inputs from all coauthors; B.T. and D.A.M. designed research with inputs from all coauthors; B.T. performed the neurophysiological recordings; M.F., B.T., A.D., M. H., and D.A.M. performed data analysis with inputs from all coauthors; A.D. reconstructed the neuronal morphologies and performed the immunohistochemistry. We dedicate this paper to the memory of Dr Babak Tahvildari.

Supplementary Material

Supplementary material can be found at: http://www.cercor.oxfordjournals.org/.

Funding

This work was supported in part by NIH Grant MH60013, NIH Grant MH61492 awarded to M.E.H. and in part by NIH Grant awarded to D.A.M. and by the Kavli Institute for Neuroscience at Yale. B.T. was an awardee of The Robert Leet and Clara Guthrie Patterson Trust Postdoctoral Fellowship, Bank of America, Trustee.

Notes

We are grateful to Drs Yusuke Tsuno, Marianne Bezaire, Todd Gillette, and all the members of Dr Hasselmo's laboratory for helpful discussions and comments on this work. We thank William (Bill) Chapman, Matthew Hapenney, and Arjun P. Reddy for help with the data analysis. *Conflict of Interest*: None declared.

References

Alitto HJ, Dan Y. 2013. Cell-type-specific modulation of neocortical activity by basal forebrain input. Front Syst Neurosci. 6:79.

Alonso A, Klink R. 1993. Differential electroresponsiveness of stellate and pyramidal-like cells of medial entorhinal cortex layer II. J Neurophysiol. 70(1):128–143.

Alonso A, Llinás RR. 1989. Subthreshold Na^+-dependent theta-like rhythmicity in stellate cells of entorhinal cortex layer II. Nature. 342(6246):175–177.

Armañanzas R, Ascoli GA. 2015. Towards the automatic classification of neurons. Trends Neurosci. 38(5):307–318.

Ascoli GA, Alonso-Nanclares L, Anderson SA, Barrionuevo G, Benavides-Piccione R, Burkhalter A, Buzsáki G, Cauli B, Defelipe J, Fairén A, et al. 2008. Petilla terminology: nomenclature of features of GABAergic interneurons of the cerebral cortex. Nat Rev Neurosci. 9:557–568.

Ascoli GA, Donohue DE, Halavi M. 2007. NeuroMorpho.Org: a central resource for neuronal morphologies. J Neurosci. 27 (35):9247–9251.

Beed P, Gundlfinger A, Schneiderbauer S, Song J, Böhm C, Burgalossi A, Brecht M, Vida I, Schmitz D. 2013. Inhibitory gradient along the dorsoventral axis in the medial entorhinal cortex. Neuron. 79(6):1197–1207.

Bezaire MJ, Soltesz I. 2013. Quantitative assessment of CA1 local circuits: knowledge base for interneuron-pyramidal cell connectivity. Hippocampus. 23(9):751–785.

Boehlen A, Heinemann U, Erchova I. 2010. The range of intrinsic frequencies represented by medial entorhinal cortex stellate cells extends with age. J Neurosci. 30:4585–4589.

Brandon MP, Bogaard AR, Libby CP, Connerney MA, Gupta K, Hasselmo ME. 2011. Reduction of theta rhythm dissociates grid cell spatial periodicity from directional tuning. Science. 332(6029):595–599.

Brandon MP, Bogaard AR, Schultheiss NW, Hasselmo ME. 2013. Segregation of cortical head direction cell assemblies on alternating theta cycles. Nat Neurosci. 16(6):739–748.

Breiman L, Friedman JH, Olshen RA, Stone CJ. 1984. Classification and Regression Trees. Belmont, CA: Wadsworth.

Brock G, Pihur V, Datta S, Datta S. 2008. clValid: An R Package for Cluster Validation. J Stat Softw. 25(4). Available from: URL http://www.jstatsoft.org/v25/i04 (24 May 2016, date last accessed).

Buckmaster PS, Alonso A, Canfield DR, Amaral DG. 2004. Dendritic morphology, local circuitry, and intrinsic electrophysiology of principal neurons in the entorhinal cortex of macaque monkeys. J Comp Neurol. 470(3):317–329.

Buetfering C, Allen K, Monyer H. 2014. Parvalbumin interneurons provide grid cell-driven recurrent inhibition in the medial entorhinal cortex. Nat Neurosci. 17(5):710–718.

Burak Y, Fiete IR. 2009. Accurate path integration in continuous attractor network models of grid cells. PLoS Comput Biol. 5: e1000291.

Burgess N, Barry C, O'Keefe J. 2007. An oscillatory interference model of grid cell firing. Hippocampus. 17:801–812.

Butt SJ, Fuccillo M, Nery S, Noctor S, Kriegstein A, Corbin JG, Fishell G. 2005. The temporal and spatial origins of cortical interneurons predict their physiological subtype. Neuron. 48 (4):591–604.

Buzsaki G, Moser EI. 2013. Memory, navigation and theta rhythm in the hippocampal-entorhinal system. Nat Neurosci. 16:130–138.

Cannon RC, Turner DA, Pyapali GK, Wheal HV. 1998. An on-line archive of reconstructed hippocampal neurons. J Neurosci Methods. 84(1–2):49–54.

Canto CB, Witter MP. 2012a. Cellular properties of principal neurons in the rat entorhinal cortex. II. The medial entorhinal cortex. Hippocampus. 22(6):1277–1299.

Canto CB, Witter MP. 2012b. Cellular properties of principal neurons in the rat entorhinal cortex. I. The lateral entorhinal cortex. Hippocampus. 22(6):1256–1276.

Cardin JA, Carlén M, Meletis K, Knoblich U, Zhang F, Deisseroth K, Tsai LH, Moore CI. 2009. Driving fast-spiking cells induces gamma rhythm and controls sensory responses. Nature. 459 (7247):663–667.

Caterina MJ, Schumacher MA, Tominaga M, Rosen TA, Levine JD, Julius D. 1997. The capsaicin receptor: a heat-activated ion channel in the pain pathway. Nature. 389(6653):816–824.

Cauli B, Audinat E, Lambolez B, Angulo MC, Ropert N, Tsuzuki K, Hestrin S, Rossier J. 1997. Molecular and physiological diversity of cortical nonpyramidal cells. J Neurosci. 17(10):3894–3906.

Chen J, Sroubek J, Krishnan Y, Li Y, Bian J, McDonald TV. 2009. PKA phosphorylation of HERG protein regulates the rate of channel synthesis. Am J Physiol Heart Circ Physiol. 296: H1244–H1254.

Chittajallu R, Craig MT, McFarland A, Yuan X, Gerfen S, Tricoire L, Erkkila B, Barron SC, Lopez CM, Liang BJ, et al. 2013. Dual origins of functionally distinct O-LM interneurons revealed by differential 5-HT(3A)R expression. Nat Neurosci. 16(11):1598–1607.

Cho H, Yang YD, Lee J, Lee B, Kim T, Jang Y, Back SK, Na HS, Harfe BD, Wang F, et al. 2012. The calcium-activated chloride channel anoctamin 1 acts as a heat sensor in nociceptive neurons. Nat Neurosci. 15(7):1015–1021.

Chowdhury S, Jarecki BW, Chanda B. 2014. A molecular framework for temperature-dependent gating of ion channels. Cell. 158(5):1148–1158.

Clapham DE. 2003. TRP channels as cellular sensors. Nature. 426 (6966):517–524.

Climer JR, Newman EL, Hasselmo ME. 2013. Phase coding by grid cells in unconstrained environments: two-dimensional phase precession. Eur J Neurosci. 38:2526–2541.

Cobos I, Long JE, Thwin MT, Rubenstein JL. 2006. Cellular patterns of transcription factor expression in developing cortical interneurons. Cereb Cortex. 16(Suppl 1):i82–i88.

Connor JR, Peters A. 1984. Vasoactive intestinal polypeptide-immunoreactive neurons in rat visual cortex. Neuroscience. 12(4):1027–1044.

Couey JJ, Witoelar A, Zhang SJ, Zheng K, Ye J, Dunn B, Czajkowski R, Moser MB, Moser EI, Roudi Y, et al. 2013. Recurrent inhibitory circuitry as a mechanism for grid formation. Nat Neurosci. 16(3):318–324.

Craig MT, McBain CJ. 2015. Navigating the circuitry of the brain's GPS system: future challenges for neurophysiologists. Hippocampus. 25(6):736–743.

DeCoursey TE, Cherny VV. 1998. Temperature dependence of voltage-gated H+ currents in human neutrophils, rat alveolar epithelial cells, and mammalian phagocytes. J Gen Physiol. 112(4):503–522.

Destexhe A, Hughes SW, Rudolph M, Crunelli V. 2010. Are corticothalamic UP states fragments of wakefulness? Trends Neurosci. 30(7):334–342.

Dib-Hajj SD, Yang Y, Waxman SG. 2008. Genetics and molecular pathophysiology of Na(v)1.7-related pain syndromes. Adv Genet. 63:85–110.

Dickson CT, Magistretti J, Shalinsky MH, Fransén E, Hasselmo ME, Alonso A. 2000. Properties and role of I(h) in the pacing of subthreshold oscillations in entorhinal cortex layer II neurons. J Neurophysiol. 83(5):2562–2579.

Dickson CT, Mena AR, Alonso A. 1997. Electroresponsiveness of medial entorhinal cortex layer III neurons in vitro. Neuroscience. 81(4):937–950.

Doischer D, Hosp JA, Yanagawa Y, Obata K, Jonas P, Vida I, Bartos M. 2008. Postnatal differentiation of basket cells from slow to fast signaling devices. J Neurosci. 28(48):12956–12968.

Domnisoru C, Kinkhabwala AA, Tank DW. 2013. Membrane potential dynamics of grid cells. Nature. 495(7440):199–204.

Dunstan RW, Wharton KA Jr, Quigley C, Lowe A. 2011. The use of immunohistochemistry for biomarker assessment–can it compete with other technologies? Toxicol Pathol. 39 (6):988–1002.

Duque A, Gazula V, Kaczmarek LK. 2013. Expression of Kv1.3 potassium channels regulates density of cortical interneurons. Dev Neurobiol. 73(11):10.1002.

Eggink H, Mertens P, Storm E, Giocomo LM. 2013. Hyperpolarization-activated cyclic nucleotide-gated 1 independent grid cell-phase precession in mice. Hippocampus. 24:249–256.

Egorov AV, Hamam BN, Fransen E, Hasselmo ME, Alonso AA. 2002. Graded persistent activity in entorhinal cortex neurons. Nature. 420:173–178.

Erchova I, Kreck G, Heinemann U, Herz AV. 2004. Dynamics of rat entorhinal cortex layer II and III cells: characteristics of membrane potential resonance at rest predict oscillation properties near threshold. J Physiol. 560(Pt 1):89–110.

Ferrante M. 2012. Dynamical Multiscale Models to Formulate Testable Predictions of Neuronal Computational Properties. Ph.D. Dissertation. George Mason Univ., Fairfax, VA, USA. Advisor Giorgio A. Ascoli. AAI3503977, ISBN: 978–1-267-27837-1.

Ferrante M, Ascoli GA. 2015. Distinct and synergistic feedforward inhibition of pyramidal cells by basket and bistratified interneurons. Front Cell Neurosci. 9:439.

Ferrante M, Blackwell KT, Migliore M, Ascoli GA. 2008. Computational models of neuronal biophysics and the characterization of potential neuropharmacological targets. Curr Med Chem. 15(24):2456–2471.

Ferrante M, Migliore M, Ascoli GA. 2009. Feed-forward inhibition as a buffer of the neuronal input-output relation. Proc Natl Acad Sci USA. 106(42):18004–9.

Ferrante M, Migliore M, Ascoli GA. 2013. Functional impact of dendritic branch-point morphology. J Neurosci. 33(5): 2156–2165.

Ferrante M, Shay CF, Tsuno Y, William Chapman G, Hasselmo ME. 2016. Post-inhibitory rebound spikes in rat medial entorhinal layer II/III principal cells: in vivo, in vitro, and computational modeling characterization. Cereb Cortex. 129:83–98.

Fishell G, Rudy B. 2011. Mechanisms of inhibition within the telencephalon: "where the wild things are". Annu Rev Neurosci. 34:535–567.

Fransén E, Tahvildari B, Egorov AV, Hasselmo ME, Alonso AA. 2006. Mechanism of graded persistent cellular activity of entorhinal cortex layer v neurons. Neuron. 49(5):735–746.

Fu Y, Tucciarone JM, Espinosa JS, Sheng N, Darcy DP, Nicoll RA, Huang ZJ, Stryker MP. 2014. A cortical circuit for gain control by behavioral state. Cell. 156:1139–1152.

Fyhn M, Molden S, Witter MP, Moser EI, Moser MB. 2004. Spatial representation in the entorhinal cortex. Science. 305 (5688):1258–1264.

Garden DL, Dodson PD, O'Donnell C, White MD, Nolan MF. 2008. Tuning of synaptic integration in the medial entorhinal cortex to the organization of grid cell firing fields. Neuron. 60 (5):875–889.

Giocomo LM, Hasselmo ME. 2009. Knock-out of HCN1 subunit flattens dorsal-ventral frequency gradient of medial entorhinal neurons in adult mice. J Neurosci. 29(23):7625–7630.

Giocomo LM, Hussaini SA, Zheng F, Kandel ER, Moser MB, Moser EI. 2011a. Grid cells use hcn1 channels for spatial scaling. Cell. 147:1159–1170.

Giocomo LM, Moser M-B, Moser EI. 2011b. Computational models of grid cells. Neuron. 71:589–603.

Giocomo LM, Zilli EA, Fransen E, Hasselmo ME. 2007. Temporal frequency of subthreshold oscillations scales with entorhinal grid cell field spacing. Science. 315:1719–1722.

Goldberg EM, Clark BD, Zagha E, Nahmani M, Erisir A, Rudy B. 2008. K+ channels at the axon initial segment Dampen near-threshold excitability of neocortical fast-spiking GABAergic interneurons neuron. Neuron. 58(3):387–400.

Gonchar Y, Wang Q, Burkhalter A. 2008. Multiple distinct subtypes of GABAergic neurons in mouse visual cortex identified by triple immunostaining. Front Neuroanat. 1:3.

Gonzalez-Sulser A, Parthier D, Candela A, McClure C, Pastoll H, Garden D, Sürmeli G, Nolan MF. 2014. GABAergic projections from the medial septum selectively inhibit interneurons in the medial entorhinal cortex. J Neurosci. 34(50):16739–16743.

Guerra L, McGarry LM, Robles V, Bielza C, Larrañaga P, Yuste R. 2011. Comparison between supervised and unsupervised classifications of neuronal cell types: a case study. Dev Neurobiol. 71(1):71–82.

Haas JS, White JA. 2002. Frequency selectivity of layer II stellate cells in the medial entorhinal cortex. J Neurophysiol. 88:2422–2429.

Hadzipasic M, Tahvildari B, Nagy M, Bian M, Horwich AL, McCormick DA. 2014. Selective degeneration of a physiological subtype of spinal motor neuron in mice with SOD1-linked ALS. Proc Natl Acad Sci USA. 111(47):16883–8.

Hafting T, Fyhn M, Bonnevie T, Moser MB, Moser EI. 2008. Hippocampus-independent phase precession in entorhinal grid cells. Nature. 453(7199):1248–1252.

Hafting T, Fyhn M, Molden S, Moser MB, Moser EI. 2005. Microstructure of a spatial map in the entorhinal cortex. Nature. 436(7052):801–806.

Hajós F, Zilles K, Schleicher A, Kálmán M. 1988. Types and spatial distribution of vasoactive intestinal polypeptide (VIP)-containing synapses in the rat visual cortex. Anat Embryol (Berl). 178(3):207–217.

Hájos N, Mody I. 2009. Establishing a physiological environment for visualized in vitro brain slice recordings by increasing oxygen supply and modifying aCSF content. J Neurosci Methods. 183(2):107–113.

Hasselmo ME. 2013. Neuronal rebound spiking, resonance frequency and theta cycle skipping may contribute to grid cell firing in medial entorhinal cortex. Philos Trans R Soc Lond B Biol Sci. 369(1635):20120523.

Hasselmo ME, Shay CF. 2014. Grid cell firing patterns may arise from feedback interaction between intrinsic rebound spiking and transverse traveling waves with multiple heading angles. Front Syst Neurosci. 8:201.

Hasselmo ME, Stern CE. 2015. Current questions on space and time encoding. Hippocampus. 25(6):744–752.

Hochbaum DR, Zhao Y, Farhi SL, Klapoetke N, Werley CA, Kapoor V, Zou P, Kralj JM, Maclaurin D, Smedemark-Margulies N, et al. 2014. All-optical electrophysiology in mammalian neurons using engineered microbial rhodopsins. Nat Methods. 11(8):825–833.

Hu H, Gan J, Jonas P. 2014. Interneurons. Fast-spiking, parvalbumin^{+} GABAergic interneurons: from cellular design to microcircuit function. Science. 345(6196):1255263.

Hutcheon B, Yarom Y. 2000. Resonance, oscillation and the intrinsic frequency preferences of neurons. Trends Neurosci. 23(5):216–222.

Ibáñez-Sandoval O, Tecuapetla F, Unal B, Shah F, Koós T, Tepper JM. 2011. A novel functionally distinct subtype of striatal neuropeptide Y interneuron. J Neurosci. 31 (46):16757–16769.

Johnson SM, Felder RB. 1993. Effects of aging on the intrinsic membrane properties of medial NTS neurons of Fischer-344 rats. J Neurophysiol. 70(5):1975–1987.

Karagiannis A, Gallopin T, Dávid C, Battaglia D, Geoffroy H, Rossier J, Hillman EM, Staiger JF, Cauli B. 2009. Classification of NPY-expressing neocortical interneurons. J Neurosci. 29 (11):3642–3659.

Karnani MM, Agetsuma M, Yuste R. 2014. A blanket of inhibition: functional inferences from dense inhibitory connectivity. Curr Opin Neurobiol. 26:96–102.

Kawaguchi Y, Katsumaru H, Kosaka T, Heizmann CW, Hama K. 1987. Fast spiking cells in rat hippocampus (CA1 region) contain the calcium-binding protein parvalbumin. Brain Res. 416(2):369–374.

Kawaguchi Y, Kubota Y. 1997. GABAergic cell subtypes and their synaptic connections in rat frontal cortex. Cereb Cortex. 7 (6):476–486.

Kawaguchi Y, Kubota Y. 1996. Physiological and morphological identification of somatostatin- or vasoactive intestinal polypeptide-containing cells among GABAergic cell subtypes in rat frontal cortex. J Neurosci. 16(8):2701–2715.

Keshavarzi S, Sullivan RK, Ianno DJ, Sah P. 2014. Functional properties and projections of neurons in the medial amygdala. J Neurosci. 34(26):8699–8715.

Klausberger T, Marton LF, O'Neill J, Huck JH, Dalezios Y, Fuentealba P, Suen WY, Papp E, Kaneko T, Watanabe M, et al. 2005. Complementary roles of cholecystokinin- and parvalbumin-expressing GABAergic neurons in hippocampal network oscillations. J Neurosci. 25(42):9782–9793.

Klink R, Alonso A. 1997. Ionic mechanisms of muscarinic depolarization in entorhinal cortex layer II neurons. J Neurophysiol. 77(4):1829–1843.

Krimer LS, Zaitsev AV, Czanner G, Kröner S, González-Burgos G, Povysheva NV, Iyengar S, Barrionuevo G, Lewis DA. 2005. Cluster analysis-based physiological classification and morphological properties of inhibitory neurons in layers 2-3 of monkey dorsolateral prefrontal cortex. J Neurophysiol. 94(5):3009–3022.

Kubota Y, Hattori R, Yui Y. 1994. Three distinct subpopulations of GABAergic neurons in rat frontal agranular cortex. Brain Res. 649:159–173.

Lee S, Hjerling-Leffler J, Zagha E, Fishell G, Rudy B. 2010. The largest group of superficial neocortical GABAergic interneurons expresses ionotropic serotonin receptors. J Neurosci. 30 (50):16796–16808.

Lee S, Kruglikov I, Huang ZJ, Fishell G, Rudy B. 2013. A disinhibitory circuit mediates motor integration in the somatosensory cortex. Nat Neurosci. 16:1662–1670.

Magistretti PJ, Morrison JH. 1998. Noradrenaline- and vasoactive intestinal peptide-containing neuronal systems in neocortex: functional convergence with contrasting morphology. Neuroscience. 24:367–378.

Maingret F, Lauritzen I, Patel AJ, Heurteaux C, Reyes R, Lesage F, Lazdunski M, Honoré E. 2000. TREK-1 is a heat-activated background K(+) channel. EMBO J. 19(11):2483–2491.

McCormick DA, Connors BW, Lighthall JW, Prince DA. 1985. Comparative electrophysiology of pyramidal and sparsely spiny stellate neurons of the neocortex. J Neurophysiol. 54 (4):782–806.

McKemy DD, Neuhausser WM, Julius D. 2002. Identification of a cold receptor reveals a general role for TRP channels in thermosensation. Nature. 416(6876):52–58.

Migliore M, Ferrante M, Ascoli GA. 2005. Signal propagation in oblique dendrites of CA1 pyramidal cells. J Neurophysiol. 94 (6):4145–4155.

Migliore M, Messineo L, Ferrante M. 2004. Dendritic Ih selectively blocks temporal summation of unsynchronized distal inputs in CA1 pyramidal neurons. J Comput Neurosci. 16(1):5–13.

Miyoshi G, Hjerling-Leffler J, Karayannis T, Sousa VH, Butt SJ, Battiste J, Johnson JE, Machold RP, Fishell G. 2010. Genetic fate mapping reveals that the caudal ganglionic eminence produces a large and diverse population of superficial cortical interneurons. J Neurosci. 30(5):1582–1594.

Mizuseki K, Sirota A, Pastalkova E, Buzsaki G. 2009. Theta oscillations provide temporal windows for local circuit computation in the entorhinal-hippocampal loop. Neuron. 64 (2):267–280.

Moran MM, Xu H, Clapham DE. 2004. TRP ion channels in the nervous system. Curr Opin Neurobiol. 14(3):362–369.

Nery S, Fishell G, Corbin JG. 2002. The caudal ganglionic eminence is a source of distinct cortical and subcortical cell populations. Nat Neurosci. 5(12):1279–1287.

Newman EL, Climer JR, Hasselmo ME. 2014. Grid cell spatial tuning reduced following systemic muscarinic receptor blockade. Hippocampus. 24:643–655.

Oliva AA Jr, Jiang M, Lam T, Smith KL, Swann JW. 2000. Novel hippocampal interneuronal subtypes identified using transgenic mice that express green fluorescent protein in GABAergic interneurons. J Neurosci. 20(9):3354–3368.

Patapoutian A, Peier AM, Story GM, Viswanath V. 2003. ThermoTRP channels and beyond: mechanisms of temperature sensation. Nat Rev Neurosci. 4(7):529–539.

Perez-Rosello T, Baker JL, Ferrante M, Iyengar S, Ascoli GA, Barrionuevo G. 2011. Passive and active shaping of unitary responses from associational/commissural and perforant path synapses in hippocampal CA3 pyramidal cells. J Comput Neurosci. 31(2):159–182.

Petersen CC, Hahn TT, Mehta M, Grinvald A, Sakmann B. 2003. Interaction of sensory responses with spontaneous depolarization in layer 2/3 barrel cortex. Proc Natl Acad Sci USA. 100 (23):13638–13643.

Pfeffer CK, Xue M, He M, Huang ZJ, Scanziani M. 2013. Inhibition of inhibition in visual cortex: the logic of connections between molecularly distinct interneurons. Nat Neurosci. 16 (8):1068–1076.

Pi HJ, Hangya B, Kvitsiani D, Sanders JI, Huang ZJ, Kepecs A. 2013. Cortical interneurons that specialize in disinhibitory control. Nature. 503:521–524.

Pike FG, Goddard RS, Suckling JM, Ganter P, Kasthuri N, Paulsen O. 2000. Distinct frequency preferences of different types of rat hippocampal neurones in response to oscillatory input currents. J Physiol. 529(Pt 1):205–213.

Porter JT, Cauli B, Staiger JF, Lambolez B, Rossier J, Audinat E. 1998. Properties of bipolar VIPergic interneurons and their excitation by pyramidal neurons in the rat neocortex. Eur J Neurosci. 10:3617–3628.

Pouille F, Marin-Burgin A, Adesnik H, Atallah BV, Scanziani M. 2009. Input normalization by global feedforward inhibition expands cortical dynamic range. Nat Neurosci. 12(12): 1577–1585.

Pusch M, Ludewig U, Jentsch TJ. 1997. Temperature dependence of fast and slow gating relaxations of ClC-0 chloride channels. J Gen Physiol. 109(1):105–116.

Rudy B, Fishell G, Lee S, Hjerling-Leffler J. 2011. Three groups of interneurons account for nearly 100% of neocortical GABAergic neurons. Dev Neurobiol. 71(1):45–61.

Salkoff DB, Zagha E, Yüzgeç Ö, McCormick DA. 2015. Synaptic mechanisms of tight spike synchrony at gamma frequency in cerebral cortex. J Neurosci. 35(28):10236–10251.

Sanchez-Vives MV, McCormick DA. 2000. Cellular and network mechanisms of rhythmic recurrent activity in neocortex. Nat Neurosci. 3(10):1027–1034.

Santi CM, Ferreira G, Yang B, Gazula VR, Butler A, Wei A, Kaczmarek LK, Salkoff L. 2006. Opposite regulation of Slick and Slack K+ channels by neuromodulators. J Neurosci. 26:5059–5068.

Shay CF, Ferrante M, Chapman GW, Hasselmo ME. 2015. Rebound Spiking in Layer II Medial Entorhinal Cortex Stellate Cells: Possible Mechanism of Grid Cell Function. Neurobiol Learn Mem. doi:10.1016/j.nlm.2015.09.004.

Siddiq A, Miyazaki T, Takagishi Y, Kanou Y, Hayasaka S, Inouye M, Seo H, Murata Y. 2001. Expression of ZAKI-4 messenger ribonucleic acid in the brain during rat development and the effect of hypothyroidism. Endocrinology. 142(5):1752–1759.

Solstad T, Boccara CN, Kropff E, Moser MB, Moser EI. 2008. Representation of geometric borders in the entorhinal cortex. Science. 322(5909):1865–1868.

Sosulina L, Meis S, Seifert G, Steinhäuser C, Pape HC. 2006. Classification of projection neurons and interneurons in the rat lateral amygdala based upon cluster analysis. Mol Cell Neurosci. 33(1):57–67.

Steriade M, Nuñez A, Amzica F. 1993. A novel slow (<1 Hz) oscillation of neocortical neurons in vivo: depolarizing and hyperpolarizing components. J Neurosci. 13(8):3252–3265.

Steriade M, Timofeev I, Grenier F. 2001. Natural waking and sleep states: a view from inside neocortical neurons. J Neurophysiol. 85(5):1969–1985.

Suzuki WA. 2010. Untangling memory from perception in the medial temporal lobe. Trends Cogn Sci. 14(5):195–200.

Tahvildari B, Alonso A. 2005. Morphological and electrophysiological properties of lateral entorhinal cortex layers II and III principal neurons. J Comp Neurol. 491(2):123–140.

Tahvildari B, Alonso AA, Bourque CW. 2008. Ionic basis of ON and OFF persistent activity in layer III lateral entorhinal cortical principal neurons. J Neurophysiol. 99(4):2006–2011.

Tahvildari B, Fransén E, Alonso AA, Hasselmo ME. 2007. Switching between "On" and "Off" states of persistent activity in lateral entorhinal layer III neurons. Hippocampus. 17(4):257–263.

Tahvildari B, Wölfel M, Duque A, McCormick DA. 2012. Selective functional interactions between excitatory and inhibitory cortical neurons and differential contribution to persistent activity of the slow oscillation. J Neurosci. 32(35):12165–12179.

Tang Q, Burgalossi A, Ebbesen CL, Ray S, Naumann R, Schmidt H, Spicher D, Brecht M. 2014. Pyramidal and stellate cell specificity of grid and border representations in layer 2 of medial entorhinal cortex. Neuron. 84(6):1191–1197.

Tsuno Y, Chapman GW, Hasselmo ME. 2015. Rebound spike properties of medial entorhinal cortex neurons in vivo. Eur J Neurosci. 42(11):2974–2984.

Uematsu M, Hirai Y, Karube F, Ebihara S, Kato M, Abe K, Obata K, Yoshida S, Hirabayashi M, Yanagawa Y, et al. 2008. Quantitative chemical composition of cortical GABAergic neurons revealed in transgenic venus-expressing rats. Cereb Cortex. 18(2):315–330.

Vandenberg JI, Varghese A, Lu Y, Bursill JA, Mahaut-Smith MP, Huang CL. 2006. Temperature dependence of human ether-a-go-go-related gene K+ currents. Am J Physiol Cell Physiol. 291(1):C165–C175.

Ward JH Jr. 1963. Hierarchical grouping to optimize an objective function. J Am Stat Assoc. 58(301):236–244.

Xu Q, Cobos I, De La Cruz E, Rubenstein JL, Anderson SA. 2004. Origins of cortical interneuron subtypes. J Neurosci. 24 (11):2612–2622.

Xu H, Jeong HY, Tremblay R, Rudy B. 2013. Neocortical somatostatin-expressing GABAergic interneurons disinhibit the thalamorecipient layer 4. Neuron. 77(1):155–167.